Multitechnique testing of the viscous decretion disk model

I. The stable and tenuous disk of the late-type Be star β CMi[*]

R. Klement[1], A. C. Carciofi[2], Th. Rivinius[3], D. Panoglou[2], R. G. Vieira[2], J. E. Bjorkman[4], S. Štefl[**], C. Tycner[5],
D. M. Faes[2], D. Korčáková[1], A. Müller[3], R. T. Zavala[6], and M. Curé[7]

[1] Astronomical Institute of Charles University, Charles University in Prague, V Holešovičkách 2, 180 00 Prague 8
   e-mail: robertklement@gmail.com
[2] Instituto de Astronomia, Geofísica e Ciências Atmosféricas, Universidade de São Paulo, Rua do Matão 1226, Cidade Universitária,
   05508-900, São Paulo, SP, Brazil
[3] European Organisation for Astronomical Research in the Southern Hemisphere, Casilla 19001, Santiago 19, Chile
[4] Ritter Observatory, Department of Physics & Astronomy, University of Toledo, Toledo, OH 43606, UsA
[5] Department of Physics, Central Michigan University, Mount Pleasant, MI 48859, USA
[6] US Naval Observatory, Flagstaff Station, 10391 W. Naval Observatory Rd., Flagstaff, AZ 86001
[7] Instituto de Física y Astronomía, Facultad de Ciencias, Universidad de Valparaíso, Casilla 5030, Valparaíso, Chile

ABSTRACT

Context. The viscous decretion disk (VDD) model is able to explain most of the currently observable properties of the circumstellar disks of Be stars. However, more stringent tests, focusing on reproducing multitechnique observations of individual targets via physical modeling, are needed to study the predictions of the VDD model under specific circumstances. In the case of nearby, bright Be star β CMi, these circumstances are a very stable low-density disk and a late-type (B8Ve) central star.
Aims. The aim is to test the VDD model thoroughly, exploiting the full diagnostic potential of individual types of observations, in particular, to constrain the poorly known structure of the outer disk if possible, and to test truncation effects caused by a possible binary companion using radio observations.
Methods. We use the Monte Carlo radiative transfer code HDUST to produce model observables, which we compare with a very large set of multitechnique and multiwavelength observations that include ultraviolet and optical spectra, photometry covering the interval between optical and radio wavelengths, optical polarimetry, and optical and near-IR (spectro)interferometry.
Results. A parametric VDD model with radial density exponent of $n = 3.5$, which is the canonical value for isothermal flaring disks, is found to explain observables typically formed in the inner disk, while observables originating in the more extended parts favor a shallower, $n = 3.0$, density falloff. Theoretical consequences of this finding are discussed and the outcomes are compared with the predictions of a fully self-consistent VDD model. Modeling of radio observations allowed for the first determination of the physical extent of a Be disk (35^{+10}_{-5} stellar radii), which might be caused by a binary companion. Finally, polarization data allowed for an indirect measurement of the rotation rate of the star, which was found to be $W \gtrsim 0.98$, i.e., very close to critical.

Key words. Stars: emission-line, Be – Stars: individual: β CMi – Radio continuum: stars – Submillimeter: stars – Techniques: polarimetric – Techniques: interferometric

1. Introduction

The gaseous circumstellar disks around classical Be stars are special universal laboratories. Although Be stars have been known for 150 years (Secchi 1866) and the idea of a flattened envelope has existed since 1931 (Struve 1931), consensus regarding the physical process governing the disk structure, the viscous decretion disk (VDD) model, has emerged only recently.

The VDD model, first introduced by Lee et al. (1991) and further developed by, e.g., Bjorkman (1997), Porter (1999), Okazaki (2001), and Bjorkman & Carciofi (2005), is now widely accepted as the best physical model for describing the circumstellar disks of Be stars. Among the growing evidence supporting the VDD model is the confirmation that the disks rotate in a Keplerian way (Meilland et al. 2007; Kraus et al. 2012; Wheelwright et al. 2012), allowing for the identification of viscosity as the mechanism that makes the disk grow: Viscous torques transfer angular momentum from the base of the disk outward, thus allowing the gas particles to reach progressively wider orbits. Decretion disks share most of the physical characteristics with accretion disks known, e.g., from protostars, with their name referring to the outward direction of the mass flow. The mass gets injected into the decretion disk by an as of yet not unambiguously defined mechanism, most probably a combination of nonradial pulsations, fast rotation, and possibly small-scale magnetic fields (Rivinius et al. 2013a).

Stringent tests of the VDD model focusing on reproducing the observables of individual targets are however still very few in number. The VDD model implemented in the Monte Carlo radiative transfer code HDUST (Carciofi & Bjorkman 2006, 2008)

Report Documentation Page		*Form Approved* *OMB No. 0704-0188*

Public reporting burden for the collection of information is estimated to average 1 hour per response, including the time for reviewing instructions, searching existing data sources, gathering and maintaining the data needed, and completing and reviewing the collection of information. Send comments regarding this burden estimate or any other aspect of this collection of information, including suggestions for reducing this burden, to Washington Headquarters Services, Directorate for Information Operations and Reports, 1215 Jefferson Davis Highway, Suite 1204, Arlington VA 22202-4302. Respondents should be aware that notwithstanding any other provision of law, no person shall be subject to a penalty for failing to comply with a collection of information if it does not display a currently valid OMB control number.

1. REPORT DATE **05 OCT 2015**	2. REPORT TYPE	3. DATES COVERED **00-00-2015 to 00-00-2015**
4. TITLE AND SUBTITLE **Multitechnique testing of the viscous decretion disk model**		5a. CONTRACT NUMBER
		5b. GRANT NUMBER
		5c. PROGRAM ELEMENT NUMBER
6. AUTHOR(S)		5d. PROJECT NUMBER
		5e. TASK NUMBER
		5f. WORK UNIT NUMBER
7. PERFORMING ORGANIZATION NAME(S) AND ADDRESS(ES) **US Naval Observatory, Flagstaff Station,,10391 W. Naval Observatory Rd.,,Flagstaff,,AZ, 86001**		8. PERFORMING ORGANIZATION REPORT NUMBER
9. SPONSORING/MONITORING AGENCY NAME(S) AND ADDRESS(ES)		10. SPONSOR/MONITOR'S ACRONYM(S)
		11. SPONSOR/MONITOR'S REPORT NUMBER(S)

12. DISTRIBUTION/AVAILABILITY STATEMENT
Approved for public release; distribution unlimited

13. SUPPLEMENTARY NOTES
Astronomy & Astrophysics manuscript no. aa,October 5, 2015

14. ABSTRACT

Context. The viscous decretion disk (VDD) model is able to explain most of the currently observable properties of the circumstellar disks of Be stars. However, more stringent tests, focusing on reproducing multitechnique observations of individual targets via physical modeling, are needed to study the predictions of the VDD model under specific circumstances. In the case of nearby, bright Be star b CMi, these circumstances are a very stable low-density disk and a late-type (B8Ve) central star. Aims. The aim is to test the VDD model thoroughly, exploiting the full diagnostic potential of individual types of observations, in particular, to constrain the poorly known structure of the outer disk if possible, and to test truncation effects caused by a possible binary companion using radio observations. Methods. We use the Monte Carlo radiative transfer code HDUST to produce model observables, which we compare with a very large set of multitechnique and multiwavelength observations that include ultraviolet and optical spectra, photometry covering the interval between optical and radio wavelengths, optical polarimetry, and optical and near-IR (spectro)interferometry. Results. A parametric VDD model with radial density exponent of n = 3.5, which is the canonical value for isothermal flaring disks is found to explain observables typically formed in the inner disk, while observables originating in the more extended parts favor a shallower, n = 3.0, density falloff. Theoretical consequences of this finding are discussed and the outcomes are compared with the predictions of a fully self-consistent VDD model. Modeling of radio observations allowed for the first determination of the physical extent of a Be disk (35+10 ????5 stellar radii), which might be caused by a binary companion. Finally, polarization data allowed for an indirect measurement of the rotation rate of the star, which was found to beW & 0:98, i.e., very close to critical.

15. SUBJECT TERMS

16. SECURITY CLASSIFICATION OF:			17. LIMITATION OF ABSTRACT	18. NUMBER OF PAGES	19a. NAME OF RESPONSIBLE PERSON
a. REPORT **unclassified**	b. ABSTRACT **unclassified**	c. THIS PAGE **unclassified**	**Same as Report (SAR)**	**36**	

was used to reproduce the violet-to-red peak ratio (V/R) spectroscopic variability along with photometry, polarimetry, and near-infrared (IR) interferometry of ζ Tau, providing firm evidence that the V/R oscillations are an effect of one-armed density waves in the disk (Carciofi et al. 2009). Other successful HDUST applications include the visual light-curve modeling of the 2008 outburst of 28 CMa along with the first determination of the viscosity parameter (Carciofi et al. 2012), and the modeling of visual and IR spectral energy distribution (SED) and visual spectropolarimetry of δ Sco (Carciofi et al. 2006). Further studies of individual stars include those of Jones et al. (2008) and Tycner et al. (2008) in which the BEDISK code (Sigut & Jones 2007) was used. Circumstantial evidence supporting the VDD model is also provided, e.g., by Haubois et al. (2012), who were able to reproduce observed light curves of Be stars with dynamical models; by Silaj et al. (2010), who reproduced generally well the observed Hα profiles of 56 Be stars; and by Touhami et al. (2011), who were able to reproduce the statistical properties of the color excesses of a sample of 130 stars. The basic characteristics of the VDD model and HDUST code are described in Sect. 3. For an extensive review on classical Be stars and their disks, see Rivinius et al. (2013a).

When studying a complex astrophysical system, such as a star irradiating a surrounding circumstellar disk, it is crucial to combine different observational techniques, as each probes different aspects of the disk physics. The combination of radiative transfer and disk dynamics governs most observables, and their disentangling is the central goal of the modeling process. The most characteristic observables of Be stars are the often double-peaked hydrogen emission lines and the disk excess IR emission due to free-free and bound-free emission in the ionized circumstellar disk. Observed optical and near-IR radiation is partially linearly polarized as a result of scattering off free electrons in the inner disk. Medium- and high-resolution differential spectrointerferometry across an emission line, such as Brγ, also shows patterns in visibilities and phases that are characteristic of circumstellar disks rotating in a Keplerian way. The combination of spectroscopic, photometric, polarimetric, and interferometric observations is therefore particularly strong for the case of circumstellar disks, removing some of the degeneracies arising from fitting single observations.

The main goal of this study is to apply the VDD model to the case of the well-known Be star β CMi and to test how well it handles arguably the largest set of multiwavelength and multitechnique observations of a Be star so far, thereby broadening the sample of detailed VDD tests applied on individual targets. The data set includes a compiled SED covering the ultraviolet (UV) to radio wavelengths, high-resolution spectroscopy of the emission lines, polarimetry, and high-resolution spectrointerferometry (see Sect. 2).

Besides being nearby, bright and therefore often observed, β CMi was chosen as the target for this study for two additional reasons. Firstly, the disk of β CMi has been been present and stable for decades. Slettebak (1982) reported "no appreciable change" in line emission in the years 1950 to 1982 and the same holds for measurements from 1989 and 1991, which were published in Hanuschik et al. (1996). This implies that the disk does not go through major mass ejection and dissipation episodes often observed in many Be stars. The absence of high-amplitude V/R variations is also evidence of no large-scale density fluctuations throughout the disk. The uncertainties arising from combining observations from different epochs should therefore be minimized. Secondly, β CMi represents one of the first detailed VDD applications to a late-type Be star (B8Ve,

Abt et al. 2002), thus enabling testing of the universality of the VDD model throughout emission line stars of the spectral class B. Moreover, it is not entirely clear whether late-type Be stars differ qualitatively from the early-type stars with respect to, e.g., the observed variability (which seems to be lower for later types) and the rotation rate (higher for later types, see Sects. 3.1 and 3.2 of Rivinius et al. 2013a).

Probing the outer reaches of the disk by analyzing radio observations is another main goal of our research. For cases nonedge-on, the SED fluxes can be interpreted as the superposition of the photospheric and disk contributions. The free-free mechanism dominates the disk opacity in the near-IR and longward, and increases with wavelength approximately as $\propto \lambda^2$. Consequently, in a typical Be disk the central parts are optically thick along the line of sight and act like a pseudophotosphere, which longward of a density-dependent λ_0 grows in size according to the approximate relation $\bar{R} \propto (\lambda/\lambda_0)^{0.41}$, where $\bar{R}$ is the pseudophotosphere radius (Vieira et al. 2015, submitted). Therefore, different wavelengths probe distinct regions of the disk (see, for instance, Fig. 2 of Rivinius et al. 2013a). In this context, radio observations are of particular interest in studying the outer parts of the disk, and may eventually impose important constraints to the disk physical size. Radio observations were used to study the structure of the outer Be disks in the pioneering works of Taylor et al. (1990), Waters et al. (1991), and Dougherty et al. (1991b), however, since then no more radio studies of Be stars were published until very recently (see Sect. 2.2).

The binary nature of β CMi is still an open question. It was suggested as a spectroscopic binary by Jarad et al. (1989); however, their data cover less than two cycles (considering their period of 218.5 days) and the spectral lines in the interval $3700 - 4700$ Å, which they used to determine the radial velocities, could be contaminated by disk emission. Their results for the radial velocities are therefore questionable and have not been confirmed. Recently, Folsom et al. (2015) reported weak V/R oscillations ($V/R = 0.98 - 1.04$) of the Hα emission line with the period of 182.83 days discovered by a spectroscopic monitoring campaign in the years $2000 - 2014$. These variations may be interpreted as arising from disk asymmetries triggered by the tidal interaction between the disk and an unseen binary companion. In this case, the V/R oscillations would be phase-locked with the binary orbit and therefore the V/R period would be equal to the binary orbital period.

Binary interaction is the only known mechanism that can truncate the disk interior to the photoevaporation radius. The so-called truncation radius represents a position in the disk where the tidal torque caused by the companion is in balance with the viscous torque. At this radius the disk is not simply cut off, but rather separated into two density regimes: Within the truncation radius the radial density decrease dependence can become shallower than an equivalent, isolated disk, and outside the truncation radius it becomes steeper, while the magnitude of this effect depends on the viscosity parameter (Okazaki et al. 2002; Panoglou et al. 2015) and on the binary mass ratio (Sect. 5). If the reported V/R variations are indeed the effect of a binary orbit, radio observations might in principle be used to detect and quantify the truncation of the disk by the companion. In view of the possible change of the density structure with respect to steady viscous decretion caused by a binary truncation or a nonsteady decretion (Haubois et al. 2012), we investigate whether steady viscous decretion provides an adequate description or whether a more complicated density structure is necessary.

Table 1. The observed IR and radio fluxes.

λ (μm)	Flux (Jy)	Instrument
9	4.892 ± 0.005	AKARI
8 – 13	3.31 ± 0.27^{a}	MIDI
11.6	2.78 ± 0.03	WISE
12	3.21 ± 0.16	IRAS
18	1.988 ± 0.061	AKARI
22.1	1.58 ± 0.03	WISE
23.7	1.47 ± 0.01	SST
25	1.52 ± 0.15	IRAS
60	0.59 ± 0.06	IRAS
71.4	4.23e-1 $\pm$ 0.51e-1	SST
870	3.35e-2 $\pm$ 0.65e-2	APEX/LABOCA
1100	3.7e-2 $\pm$ 0.6e-2	JCMT
3265	9.6e-3 $\pm$ 0.6e-3	CARMA
20000	0.69e-3 $\pm$ 0.10e-3	VLA

Notes.
[a] The flux value is for the central N-band wavelength of 10.5 μm

The last goal is to look for observable signatures of the disk nonisothermality, which is expected from theory. Be disks become nonisothermal because the inner, dense parts of the disk are optically thick to the photoionizing stellar radiation, causing an initial temperature decrease in the radial direction. As the density gets lower further from the star, the temperature rises to about 60% of the stellar effective temperature and the disk becomes roughly isothermal. The temperature structure is expected to have an effect on the density structure of the disk, which then affects the observables (Carciofi & Bjorkman 2008).

In Sect. 2 the observations are described, while Sect. 3 briefly describes the adopted modeling procedure. In Sect. 4 the model predictions are presented and with their help the observations are interpreted. The conclusions follow.

2. Observations

2.1. Optical and IR photometry

Standard Johnson *UBVRI* photometry was taken from the catalog of Ducati (2002). The *UBVRI* photometry was dereddened with the reddening curve of Cardelli et al. (1989) using the extinction coefficient $R_V = 3.1$ and the interstellar color excess $E[B - V] = 0.01$ adopted from the analysis of Dougherty et al. (1994). The overall reddening effects are found to be very weak (and negligible longward of 7000 Å), as is also indicated by the very low extinction toward β CMi ($A_V = 0.05$ according to Wheelwright et al. 2012).

IR photometry in filters *JHKLM* was adopted from Dougherty et al. (1991a). We also make use of the color-corrected IRAS measurements of β CMi published in Coté & Waters (1987). The remaining IR photometry was taken from the published measurements from the AKARI/IRC mid-IR all-sky Survey (Ishihara et al. 2010), from the Spitzer Space Telescope (SST; Su et al. 2006) and from the Wide-field Infrared Survey Explorer (WISE; Cutri & et al. 2014). Finally, we use the N-band flux calibrated spectrum ($R = 30$) measured by the VLTI/MIDI interferometer. The compiled IR data set is listed in Table 1.

2.2. Radio measurements

Radio observations of Be stars have been very scarce throughout decades past. However, recent years saw a great technological improvement in the instruments allowing for precise measurements even of very low fluxes. We briefly discuss the historic measurements and then describe our own from recent years.

Already in the late eighties, several Be stars including β CMi were detected at 2 cm wavelength by the Very Large Array (VLA; Taylor et al. 1990) and at mm wavelengths by the James Clerk Maxwell Telescope (JCMT; Waters et al. 1991). We use the published JCMT and VLA data in our analysis (see the respective references for the description of the data). To our knowledge, these had been the only radio observations of Be stars up until a few years ago, when 28 CMa was observed by the Atacama Pathfinder Experiment (APEX) millimeter telescope (Štefl et al. 2011) and δ Sco was observed by APEX and by the Combined Array for Research in Millimeter-wave Astronomy (CARMA, Štefl et al. 2012). More recently, we used the APEX bolometer camera LABOCA (Siringo et al. 2009) and the CARMA array (Bock et al. 2006) in its photometric mode to observe β CMi. The sub-mm and radio observations are included in Table 1.

The APEX/LABOCA camera operates at the central frequency of 345 GHz, corresponding to the wavelength of 870 μm with a bandwidth of 150 μm. It consists of a 295-channel bolometer array laid out in concentric hexagons around a central channel. The sub-mm radiation is absorbed by a heat-sensitive semi-conductor, which measures temperature variations of a thin titanium film. Our measurement consists of five scans with a total integration time of 53.8 min. The data were reduced with the help of the free reduction software CRUSH[1] version 2.20-3 (Kovács 2008).

The CARMA observations were executed with the 15-antenna subarray (nine 6.1-m and six 10.4-m diameter antennas) in the D configuration, in which the distances between the individual antennas are 11–150 m. The central frequency of the observations was ∼100 GHz (∼3 mm) with the bandwidth of ∼500 MHz. The total integration time including the calibrators was 2.60 hours. The data were reduced using the MIRIAD software package[2].

2.3. Spectroscopy

The spectral coverage of the compiled SED is extended into ultraviolet (UV) wavelengths by including spectra measured by the International Ultraviolet Explorer (IUE)[3]. We observed β CMi by IUE five times in high dispersion mode with the total spectral coverage of 1150 – 3350 Å. The spectra were averaged and then dereddened with the same approach as the optical photometry with the reddening curve updated for the near-UV according to O'Donnell (1994). Strong reddening is usually indicated by an interstellar absorption feature around 2200 Å. The fact that this feature is absent from the observed spectra is a further indication of low extinction toward β CMi and overall weak reddening effects.

In the optical region, the Johnson *UBVRI* photometry is complemented with several flux-calibrated low-resolution spectra covering the interval 3200 – 10500 Å measured by the

---

[1] http://www.submm.caltech.edu/~sharc/crush/index.html
[2] http://carma.astro.umd.edu/miriad/
[3] https://archive.stsci.edu/iue/

Table 2. Spectroscopic data set.

Date	Telescope	Instrument	No. of spectra	R	Spectral range (Å)
1986-04-05 – 1987-12-05	IUE	IUE_SWP_HL	4	18 000	1150 – 1975
1987-02-10	IUE	IUE_LWP_HL	1	13 000	1850 – 3350
1995-02-08 – 2000-02-12	PBO 36" telescope	HPOL	3	600	3200 -10500
2001-11-16 – 2007-01-08	Ondřejov 2 m	coudé spectr.	11	12 500	6300 – 6700
2004-08-01 – 2004-09-01	ESO - La Silla 2.2 m	FEROS	2	48 000	3600 – 9200
2007-01-08 – 2014-02-23	Ondřejov 2 m	coudé spectr.	9	18 500	4760 – 5000
2008-01-26	Meade LX200	LHIRES	1	17 000	6300 – 6700
2009-02-14	C11	LHIRES	1	17 000	6300 – 6700
2009-12-31 – 2010-04-23	VLTI	AMBER	2	12 000	21580 – 21760
2010-01-16	Takahashi CN212	LHIRES	1	15 000	6300 – 6700
2010-10-29	C11	LHIRES	1	17 000	6300 – 6700
2011-10-20 – 2013-09-26	OPD 1.6 m	ECass	9	5 000	6120 – 6880
2011-11-05 – 2011-11-11	CFHT 3.6 m	ESPaDOnS	80	68 000	3700 - 9000
2013-12-09 – 2014-11-18	OPD 1.6 m	MUSICOS	3	30 000	5020 – 9020
2013-02-08 – 2014-02-23	Ondřejov 2 m	coudé spectr.	7	12 500	6300 – 6700
2013-11-09 – 2014-02-23	Ondřejov 2 m	coudé spectr.	3	16 500	4280 – 4500

HPOL spectropolarimeter[4] mounted on the Pine Bluff Observatory (PBO) 36" telescope. As the absolute flux calibration of the spectra is not reliable, however, only the shape of the spectra was used. The individual measurements were scaled to the V-band magnitude before they were averaged and dereddened.

The spectroscopic observations of hydrogen Balmer emission lines ($R = 5000 – 30000$) in the $2001 – 2014$ interval were carried out using the slit spectrograph mounted at the coudé focus of Ondřejov 2 m telescope in the Czech Republic and the Cassegrain (ECass) and MUSICOS spectrographs at the 1.6 m telescope at the Observatório Pico dos Dias (OPD) in Brazil. The gaps in the time coverage were filled in by several amateur spectra from the BeSS database[5]. The Balmer lines are complemented with Brγ profiles extracted from two sets of AMBER interferometric measurements (Sect. 2.5). Overall, the line profiles show only small-scale temporal variability, although some show a weak V/R assymetry, in line with the results of Folsom et al. (2015). In Fig. 1 we show the Ondřejov and AMBER line profiles, the averages of which were used for the modeling process.

Two spectra from the high-resolution ($R = 48\,000$) fiber-fed spectrograph FEROS (Kaufer et al. 1999), mounted at the 2.2 m ESO telescope at the La Silla observatory, Chile and a set of spectroscopic measurements from the ESPaDOnS[6] echelle spectrograph ($R = 68\,000$), installed at the 3.6 m Canada-France-Hawaii Telescope (CFHT) in Hawaii, USA, allowed us to investigate the whole spectrum in the $3600 – 9200$ Å range.

The information on the spectroscopic data set is summarized in Table 2.

2.4. Linear polarimetry

β CMi was observed by the HPOL Spectropolarimeter mounted on the PBO 36" telescope six times during the years $1991 – 2005$. The first measurement was done with a Reticon dual array detector, while a CCD detector was used for the remaining scans. The wavelength coverage of the CCD observations is $3200 – 10500$ Å with a spectral bin size ~ 10 Å.
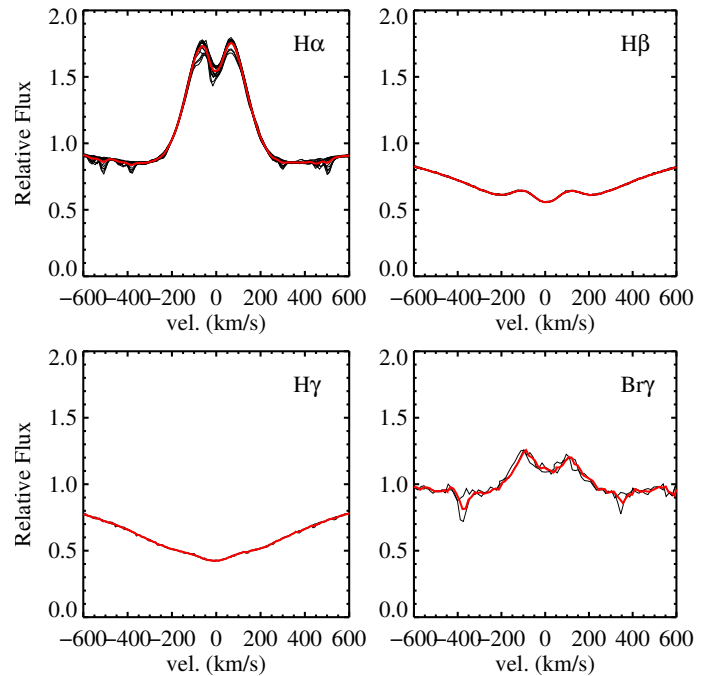
Fig. 1. Balmer line profiles from Ondřejov and Brγ profile from AMBER (black) overplotted with their averages (red), which were subsequently used in the modeling process. Telluric features can be seen in most of the Hα and Brγ profiles.

Recent broadband polarimetric measurements in the Johnson filters *BVRI* were obtained on five observing nights during the years $2011 – 2014$ at 1.6 m telescope of the OPD observatory in Brazil (Table 3, available electronically only). For the instrument description, observing setup and calibration and reduction procedures see Sect. 2 of Carciofi et al. (2007) and references therein.

As discussed in Sects. 2.1 and 2.3, the interstellar extinction toward β CMi is almost negligible, therefore, we perform no corrections for the interstellar polarization.

---

[4] `http://archive.stsci.edu/hpol/`
[5] `http://basebe.obspm.fr/basebe/`
[6] `http://www.ast.obs-mip.fr/projets/espadons/espadons.html`

Table 4. Interferometric observations from VLTI and CHARA.

Date	Instrument	Spectral band	R	NP[a]	Telescope configuration
2008-12-02	MIRC	H	35	1	S1-E1-W1-W2
2008-12-17	MIDI	N	30	1	UT1-UT4
2009-01-11	MIDI	N	30	1	UT1-UT4
2009-11-10	MIRC	H	35	3	S1-E1-W1-W2
2009-12-31	AMBER	K	12 000	1	UT1-UT2-UT3
2010-04-23	AMBER	K	12 000	1	K0-G1-A0
2010-10-30	CLIMB	K'	-	2	S2-W1-W2
2010-11-02	MIRC	H	35	3	S1-E1-W1-W2
2010-11-03	MIRC	H	35	2	S2-E2-W1-W1
2010-12-02	CLIMB	K'	-	1	S1-E2-W1
2010-12-03	CLIMB	K'	-	4	S2-E2-W2
2010-12-14	MIRC	H	35	1	S1-E2-W1-W2
2013-10-21	MIDI	N	30	1	UT1-UT4
2014-03-06	FSU-A	K	-	2	J3-K0, G1-A1
2014-03-07	FSU-A	K	-	1	K0-A1

Notes.
[a] Number of pointings obtained on the science star.

2.5. Interferometry

The interferometric observations were obtained at three interferometric facilities: Very Large Telescope Interferometer (VLTI) at the Paranal observatory in Chile, Center for High Angular Resolution Astronomy (CHARA) at the Mount Wilson Observatory in California, USA, and the Navy Precision Optical Interferometer (NPOI) located in Arizona, USA. The VLTI instruments include the 2-telescope beam combiners PRIMA FSU-A (Sahlmann et al. 2009) and MIDI (Leinert et al. 2003) and the 3-telescope beam combiner instrument AMBER (Petrov et al. 2007). We also observed β CMi for two nights (May 1 – May 3, 2014) with the 4-telescope beam combiner PIONIER (Le Bouquin et al. 2011), but these measurements were mostly lost due to bad weather conditions. The CHARA instruments used are the 4 to 6-telescope beam combiner MIRC (Monnier et al. 2006) and a 3-beam combiner CLIMB (Sturmann et al. 2010). The AMBER, MIRC, and CLIMB data were already analyzed by Kraus et al. (2012) and part of the MIDI observations was published in Meilland et al. (2009). The observation logs for interferometric observations from VLTI and CHARA are listed in Table 4 and the full NPOI data set is given in Table 5 (available electronically only).

The former PRIMA (Phase-Referenced Imaging and Microarcsecond Astrometry) facility at VLTI consisted of two identical fringe sensor units (called FSU-A and FSU-B) but only FSU-A was publicly offered for observations. The FSU-A operates in the K-band between 2.0 μm and 2.5 μm. The light is chromatically dispersed over five spectral pixels. Three visibility measurements were obtained with pairs of 1.8 m Auxiliary Telescopes (ATs). For more details on the observing setup and the reduction procedure, see Sect. 4 of Müller et al. (2014).

The MIDI data consist of three measurements executed with pairs of 8.2 m Unit Telescopes (UTs) with spectral dispersion R = 30 across the N-band (8 – 13 μm). For more details on the data acquisition and reduction, see Meilland et al. (2009) and references therein.

The AMBER observations were obtained in the high spectral resolution mode (HR mode, R = 12 000) in the K-band spectral region centered around the hydrogen Brγ line ($\lambda_{Br\gamma}^{vacuum}$ = 2.166078 μm). The pointing from December 31, 2009 was obtained with three 8.2 m UTs, while for the observation from April 23, 2010 three 1.8 m ATs were used. For our purposes, we rereduced the data using the amdlib V3.0 data reduction software (Tatulli et al. 2007; Chelli et al. 2009). As absolute calibration of the AMBER data is not reliable, we normalized the continuum region and used the differential visibilities and phases for our analysis. As the measurement error for all data points we used the standard deviation computed from the continuum region. For more details on the observing setup and the reduction procedure see Sect. 2 of Kraus et al. (2012).

The observations from MIRC were obtained with low spectral dispersion, R = 35, in the H-band continuum. The light from four 1 m telescopes was combined with the baseline lengths reaching 330 m. The CLIMB observations include eight pointings in the K'-band continuum. The observing setup and the reduction process are detailed in Sect. 2 of Kraus et al. (2012). For the uv-plane coverage of the CHARA measurements as compared to AMBER coverage, see their Fig. 1.

The NPOI is a long-baseline, multielement, optical interferometer that can combine light beams from up to six elements simultaneously (Armstrong et al. 1998). Before the fringe contrast is recorded between the beams, the light combined at the beam combiner is dispersed using a prism onto a lenslet array connected by optical fibers to a series of photon-counting avalanche photodiodes, which results in data stream from 16 spectral channels covering the wavelength range of 560 – 870 nm. For B-type stars with an Hα emission line, it allows interference fringe contrast (in the form of squared visibility) to be recorded for a single 15-nm wide spectral channel that contains the entire emission line from the circumstellar region (we refer to this as Hα channel when the 656.28 nm line is centered in the spectral channel).

The NPOI observations of β CMi utilized in this study were obtained on 40 nights from November 2010 to April 2011. The entire data set resulted in 720 unique squared visibility measurements from the Hα channel. The processing of NPOI data was conducted using a custom suite of programs developed specifically for the instrument known as the Optical Interferometer Script Data Reduction package. The processing of the raw fringe data frames follows the procedures outlined in Hummel et al. (1998) with additional bias corrections using off-fringe measurements described in Hummel et al. (2003). Furthermore, in the case of Hα-emitting sources, where the signal of interest is confined to a single spectral channel per baseline, the additional step

of removal of small channel-to-channel variations has also been conducted as described in Tycner et al. (2006) utilizing a calibrator star λ Gem (FK5 277, HR 2763). The last step of calibration of the Hα squared visibilities involved calibration with respect to the continuum channels, which are assumed to be represented by a uniform disk model with a known angular diameter (Tycner et al. 2003). In the case of β CMi, we adopted an angular diameter of the central star of 0.675 mas, which was obtained based on a Hipparcos distance of 49.6 pc (van Leeuwen 2007), the best-fit value for stellar polar radius (R_p) of 2.8 $R_\odot$ based on UV spectrum fitting (see Sect. 4.1.1) and a multiplicative factor of 1.29, which accounts for the average effect due to the rapid stellar rotation. [7]

3. Model description

We modeled β CMi as a combination of a fast-rotating central star surrounded by a viscous decretion disk with the help of the computer code HDUST. The code HDUST uses the Monte Carlo method to solve the radiative transfer, radiative equilibrium, and statistical equilibrium in 3D geometry for arbitrary density and velocity distributions assuming pure hydrogen composition. For details on the HDUST code and the hydrodynamics of a VDD; see Carciofi & Bjorkman (2006, 2008) and Carciofi (2011).

3.1. Central star

The code HDUST takes into account both the geometrical deformation of the star due to fast rotation and the latitude-dependent flux from the stellar surface due to gravity darkening. The stellar surface itself is divided into a number of latitude bins each with its own local gravity and temperature with a corresponding Kurucz (Kurucz 1979) synthetic spectrum assigned to it.

A rotating star is fully described by five parameters: mass M, polar radius R_p, luminosity L, rotation rate W, and gravity darkening exponent β. The star is a geometrically deformed isopotential surface in the Roche approximation based on the rotation rate W, defined as $W = v_{rot}/v_{orb}$, where v_{rot} is the rotational velocity at the stellar equator and v_{orb} is the Keplerian velocity of orbiting material just above the stellar equator (Sect. 2.3.1 of Rivinius et al. 2013a). In the case of critical rotation, the parameter W becomes unity. The gravity darkening law is adopted in the classical form $T_{eff} \propto g^\beta$ (von Zeipel 1924).

Two additional geometrical parameters are needed to be able to compare the model with observations: The distance d and the inclination angle i of the spin axis of the star with respect to the observer.

3.2. The disk

The VDD model in which turbulent viscosity is responsible for the disk growth and transport of the angular momentum outward has so far been able to explain most observational aspects of the Be star disks (Bjorkman 2012).

The VDD is flaring with the following dependence of the scale height H on the distance r from the stellar surface, if one

assumes hydrostatic equilibrium and an isothermal disk

$$H(r) = H_0 \left(\frac{r}{R_e} \right)^{3/2}, \tag{1}$$

where R_e is the equatorial radius of the rotationally deformed star and $H_0 = c_s v_{orb}^{-1} R_e$ is the scale height at the base of the disk. $c_s = [(k_B T_k)/(\mu m_H)]^{1/2}$ is the isothermal sound speed, k_B is the Boltzmann constant, T_k is the gas kinetic temperature, μ is the mean molecular weight, and m_H is the mass of hydrogen atom. Haubois et al. (2012) studied the hydrodynamics of Be disks and explored how the disk surface density evolves with time in response to varying disk feeding rates. Even though a dynamically active disk can have a quite complex structure, a much simpler situation arises when the disk is fed at a constant rate for a sufficiently long time. In this case, the surface density structure of a VDD under the assumption of an isothermal gas and purely Keplerian circular orbits can be described by

$$\Sigma(r) = \frac{\dot{M} v_{orb} R_e^{1/2}}{3\pi \alpha c_s^2 r^{3/2}} \left[(R_0/r)^{1/2} - 1 \right], \tag{2}$$

where α is the viscosity parameter (assumed to be constant throughout the disk), $\dot{M}$ is the mass decretion rate, r is the distance from the stellar equator, and R_0 is an integration constant connected with the physical size of the disk (Bjorkman & Carciofi 2005). For $r \ll R_0$, the dependence of $\Sigma(r)$ becomes a power-law $\Sigma(r) \propto r^{-2}$. The disk is in hydrostatic equilibrium in the vertical direction, which in the isothermal case corresponds to Gaussian distribution. The falloff of the volume density is then

$$\rho(r,z) = \frac{\Sigma(r)}{\sqrt{2\pi} H(r)} \exp\left[-\frac{1}{2} \left(\frac{z}{H(r)} \right)^2 \right], \tag{3}$$

therefore

$$\rho \propto \Sigma/H \propto r^{-n}, \tag{4}$$

with the radial density exponent n equal to 3.5, however, the disk is not radially isothermal. Initially the temperature falls with radius to a minimum that occurs in the dense inner parts of the disk. The location of the minimum depends on the disk density; for higher densities it shifts outward. The temperature minimum results in a local change of the radial density falloff exponent n and of the flaring coefficient (Carciofi & Bjorkman 2008).

Numerical solutions (e.g., Okazaki et al. 2002) show that the disk is separated into two parts: a subsonic inner part (radial velocity $v_r \ll c_s$), where the outflow is driven by viscosity; and a transonic outer part ($v_r \gtrsim c_s$), where the outflow is driven by the gas pressure. The photoevaporation radius where the transition occurs is the so-called transonic critical radius R_c, which is on the order of hundreds of stellar radii (Krtička et al. 2011). However, what is considered to be the outer radius of a Be disk depends on whether the star is in a binary system or not. If the star is in a binary system, the disk may be truncated at the tidal radius, which can be a complicated function of the binary parameters and of the viscosity parameter α (Panoglou et al. 2015). For isolated stars or well-detached binaries, however, we expect $R_{out} \approx R_c$. Radio observations have to be used to investigate these outer parts of the disk.

---

[7] To account for the rapid stellar spin, we take the average between equatorial radius R_e = 1.49 R_p (see Table 8) and the projection of the equatorial radius due to inclination i of 43° (see Sect. 4.4), i.e., $\cos(43) = 0.731$ resulting in average effective radius of 1.29 R_p.

Table 6. Characteristics and free parameters of the adopted VDD models.

Model	Characteristics	Free parameters
Parametric	power-law radial density and vertical scale height structure	ρ_0, n, H_0 (T_k), R_{out}
Self-consistent	full solution of the viscous decretion	$\dot{M}/\alpha$, R_0, R_{out}

3.3. Modeling procedure

For the present study, we have adopted two VDD models for the disk. First we start with a simplified analytical power-law model followed by the fully self-consistent solution of steady viscous decretion. As the latter model modifies the prescribed density structure according to the temperature solution, comparing the results of the two models allows us to test how the disk non-isothermality affects the observables. Improvement of the global fit to the observations after introducing the full VDD solution would then represent an indirect observational proof of the structural changes due to the disk nonisothermality.

The first model, which we dub parametric model, is based on the isothermal VDD density structure for which the vertical distribution is Gaussian and the radial distribution is a power law in the form $\rho \propto \rho_0 r^{-n}$, where ρ_0 is the density at the base of the disk. Although this corresponds to the theoretical density structure of an isothermal disk (when $n = 3.5$), the disk itself is not isothermal as its temperature is calculated in radiative equilibrium by HDUST. Values of ρ_0 were explored in the interval $1 \times 10^{-12} - 1 \times 10^{-10}$ g cm^{-3}, which is typical for Be disks. The scale height at the base of the disk H_0 is an additional parameter, which is set by the sound speed c_s and the disk orbital speed v_{orb} (see Eq. 1). As v_{orb} is given by M, R_p, and W, only a proper choice of the kinetic temperature T_k (to calculate c_s) is needed to determine the scale height H_0. We chose the mass-averaged temperature of the disk to represent T_k.

Varying the density falloff exponent n allows us to explore a standard, isolated disk with isothermal density structure ($n = 3.5$) as well as a disk truncated by a binary companion, in which the parts inward of the truncation radius may attain a shallower density profile ($n < 3.5$). Density profiles associated with a disk that has not yet reached a quasi-steady-state configuration ($n > 3.5$, see Porter 1999; Haubois et al. 2012) were also explored (although this case is unlikely for β CMi, as its disk has been present and stable for a long period already). In our modeling, n was allowed to vary in the interval $3.0 - 4.0$.

The second, self-consistent model calculates the full solution of steady viscous decretion following Carciofi & Bjorkman (2008). In this case, the radial and vertical density structures are solved to become consistent with the temperature solution and therefore the parameters n and H_0 are no longer needed. Instead of ρ_0 describing the base density, the ratio of the mass decretion rate and the viscosity parameter $\dot{M}/\alpha$ needs to be specified (see Eq. 2). The $\dot{M}/\alpha$ parameter was chosen to correspond to the ρ_0 of the parametric model so that the resulting mass of the disk would remain approximately constant, thus allowing for a direct comparison between the models. The observables we study are only sensitive to the density scale of the disk, and do not carry any information about its radial velocity because it is much smaller than the sound speed. For this reason, the mass-loss rate $\dot{M}$ cannot be determined uniquely; we can only determine ρ_0 or equivalently the ratio $\dot{M}/\alpha$. Finally, there is an additional parameter in the form of the integration constant R_0, which was assumed to correspond roughly to the critical radius R_c given by

the approximate relation of Krtička et al. (2011), i.e.,

$$\frac{R_c}{R_e} = \frac{3}{10}\left(\frac{v_{orb}}{c_s}\right)^2.$$ (5)

The parameter R_c, calculated from the best-fit model values, is $\sim 450\ R_e$.

In both models, we also need to specify the disk outer radius R_{out}, which in the modeling context represents the outer edge of the grid used for the Monte Carlo simulation, beyond which matter is absent. This parameter allows us to explore possible truncation of the disk by a binary companion.

The basic characteristics and free parameters of the models are listed in Table 6.

3.4. Initial estimates for the central star parameters

β CMi has already been a subject of several detailed studies focusing on different observational and physical aspects. β CMi was previously studied by Saio et al. (2007), whose analysis of MOST satellite observations led to the first detection of nonradial pulsations in a late-type Be star with evidence for an almost critical rotation. Elsewhere, high-resolution spectrointerferometry and spectroscopy of β CMi was used to provide evidence of Keplerian rotation of the disk (Kraus et al. 2012; Wheelwright et al. 2012). The central star parameters adopted in these studies were used as initial constraints for our modeling.

The value of $M = 3.5\ M_\odot$ was adopted in accordance with individual literature estimates (Kraus et al. 2012; Saio et al. 2007) and stellar evolution models for the spectral type B8. Although M influences the scale height of the disk as well as the critical rotation rate, changing it over the interval $3 - 4\ M_\odot$ has little overall influence on the observables, and it was therefore kept fixed at the value of $3.5\ M_\odot$.

We explored the possible values of R_p and L in the intervals $2.4 - 3.6\ R_\odot$ and $160 - 240\ L_\odot$, respectively. The rotation rate W was assumed to be $0.7 - 1.0$, corresponding to the observed rotation rates of Be stars (Sect. 3.1 of Rivinius et al. 2013a).

Recent interferometric observations as well as theoretical developments indicate that the gravity darkening law in the classical form $T_{eff} \propto g^\beta$ with $\beta = 0.25$ is valid only in the limit of slow rotators, while in rapidly rotating stars β can be significantly lower. The recent model of Espinosa Lara & Rieutord (2011) in which the barotropic assumption (pressure dependent only on density) is relaxed is in general agreement with six interferometric measurements of the β parameter in rapid rotators, as is shown in Fig. 13 of Domiciano de Souza et al. (2014). In this work we treat the gravity darkening exponent β as a function of W, according to the model of Espinosa Lara & Rieutord (2011). However, in their model, gravity darkening is in fact not described by a power law (see their Eq. 31).

3.5. Geometrical parameters

The distance d to β CMi is 49.6 ± 0.5 pc as measured by the Hipparcos satellite (van Leeuwen 2007). As varying d in such

Table 7. Model parameters

Parameter	Best-fit value	Type	Adopted range	Ref.[a]
		Stellar parameters		
Spectral type	B8Ve			2
R_p	$2.8\,R_\odot$	free	$2.4 - 3.6\,R_\odot$	1, 3, 4
M	$3.5\,M_\odot$	fixed		4, 5
L	$185\,L_\odot$	free	$160 - 240\,L_\odot$	1, 3, 4, 5
W	$\gtrsim 0.98$	free	$0.7 - 1.0$	1, 5
β	$0.1367^{+0.0025}_{-0.0013}$	function of W		6
		Disk parameters - parametric model		
ρ_0	$2.0 \times 10^{-12}\ \mathrm{g \cdot cm^{-3}}$	free	$1.0 \times 10^{-12} - 1.0 \times 10^{-10}\ \mathrm{g \cdot cm^{-3}}$	1, 3
n	$3.0 - 3.5$	free	$3.0 - 4.0$	1
$T_k{}^b$	6500 K	fixed		1
R_{out}	$35^{+10}_{-5}\,R_e$	free	$10 - 100\,R_e$	1
		Disk parameters - self-consistent model		
$\dot{M}/\alpha$	$1.88 \times 10^{-12}\ M_\odot\,\mathrm{yr^{-1}}$	free	$1.0 \times 10^{-12} - 1.0 \times 10^{-11}$	1
R_0	$450\,R_e$	fixed		7
R_{out}	$>100\,R_e$	free	$10 - 200\,R_e$	1
		Geometrical parameters		
i	$43^{+3°}_{-2°}$	free	$35 - 50°$	1, 3, 4
d	49.6 pc	fixed		8
PA^c	$133^{+4°}_{-3°}$	free	$0 - 360°$	1

Notes. [a] References: 1 - this work; 2 - Abt et al. (2002); 3 - Wheelwright et al. (2012); 4 - Kraus et al. (2012); 5 - Saio et al. (2007); 6 - Espinosa Lara & Rieutord (2011); 7 - Krtička et al. (2011); 8 - van Leeuwen (2007). [b] Assumed to be equal to the mass-averaged temperature of the disk. [c] The projected position angle of the semimajor axis of the disk measured from north to east.

a low uncertainty interval has little effect on the model observables, d was kept fixed at the value of 49.6 pc. The inclination angle i is clearly of an intermediate value with the most precise estimate from modeling of AMBER observations being $38.5 \pm 1°$ (Kraus et al. 2012). We explored the possible values of i in the interval of $35° - 50°$.

4. Results

In this Sect. the ability of the VDD model, in the two particular formalisms adopted (parametric vs. self-consistent), to reproduce individual observations is detailed.

The fitting procedure was executed in the following way: First, the almost purely photospheric UV spectrum was used to constrain the central star parameters R_p and L. Next, the SED from IR to radio wavelengths, where the disk significantly contributes to the observed flux, was used to determine the disk parameters ρ_0 and n (or $\dot{M}/\alpha$). Finally, the spectral slope of the linear polarimetry allowed us to determine the rotation rate W (and β), while we used the interferometric shape extracted from the AMBER observations to constrain the geometrical parameter i. The resulting best-fit parameters for both models are listed in Table 7 and the derived stellar parameters are listed in Table 8.

The remaining observations were used as consistency checks for the parameters determined in the way described above. The polarization level allows us to check the consistency of i, ρ_0, and n in the inner parts of the disk. The equivalent widths of the different hydrogen lines provide us with another way to check the density structure in the various parts of the disk where the emission from the respective lines originates. The final consistency checks are provided by the observed interferometric visibilities, which measure the sizes of the corresponding emitting regions, along with the interferometric phase shifts, which de-
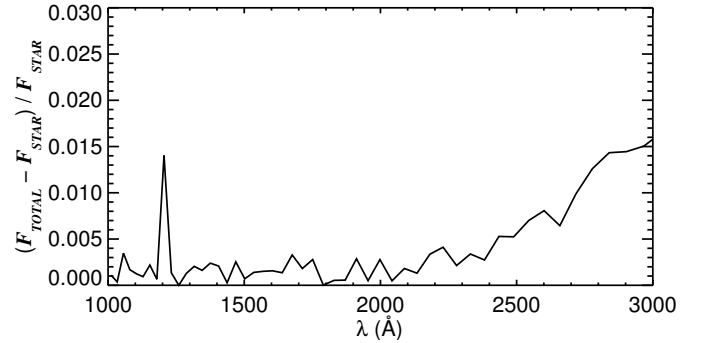
Fig. 2. The model fraction of the disk flux contribution in the 1000 – 3000 Å interval computed by dividing a model containing the disk contribution by the purely photospheric model.

Table 8. Derived model parameters

Parameter	Value
R_e/R_p	1.49
R_e	$4.17\,R_\odot$
v_{rot}	$396\ \mathrm{km \cdot s^{-1}}$
$v\sin(i)$	$270\ \mathrm{km \cdot s^{-1}}$
$\log(g)_{pole}$	4.09
T_{pole}/T_{eq}	1.91
$T_{eff,pole}$	13740 K

pend on both the velocities and densities of the corresponding parts of the disk.

Comparing the outcomes of the best-fit (parametric and self-consistent) VDD models then allows us to explore the nonisothermal effects on the observables caused by structural
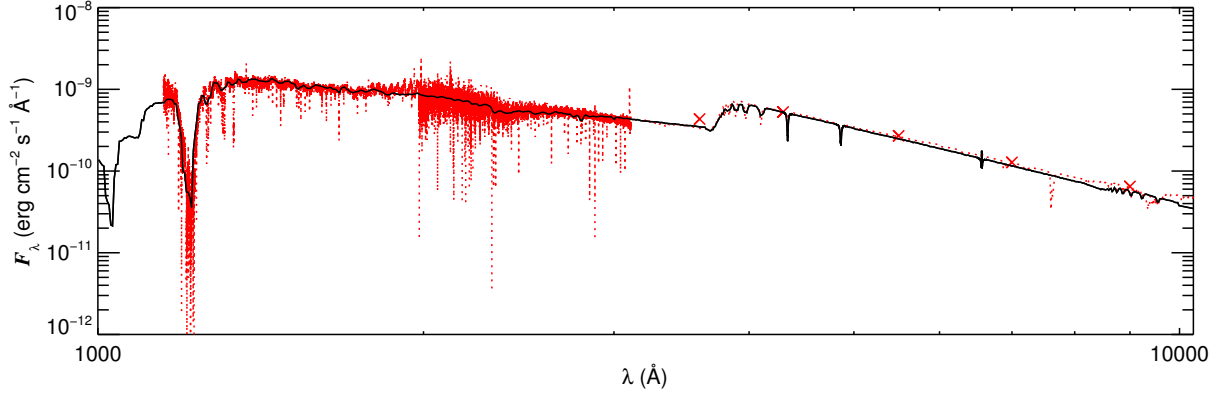
Fig. 3. The parametric ($n = 3.5$) model fit (solid black) to the average IUE and HPOL data (dotted red). The average HPOL spectrum was scaled to the V-band photometry. The broadband $UBVRI$ photometry is plotted with red crosses.

Fig. 4. *Upper:* parametric model with $n = 3.5$ (black), parametric model with $n = 3.0$ (blue), and self-consistent model (green) fit to the visual, IR, and radio SED (red plus signs). All models are plotted for $R_{\rm out} = 35\,R_{\rm p}$. The purely photospheric SED is plotted as a black dashed line. *Lower:* residuals of each model fit. The error bars are plotted where available.

changes in the disk introduced with the nonisothermal density solution. Finally, we look at the evidence in our data for the disk t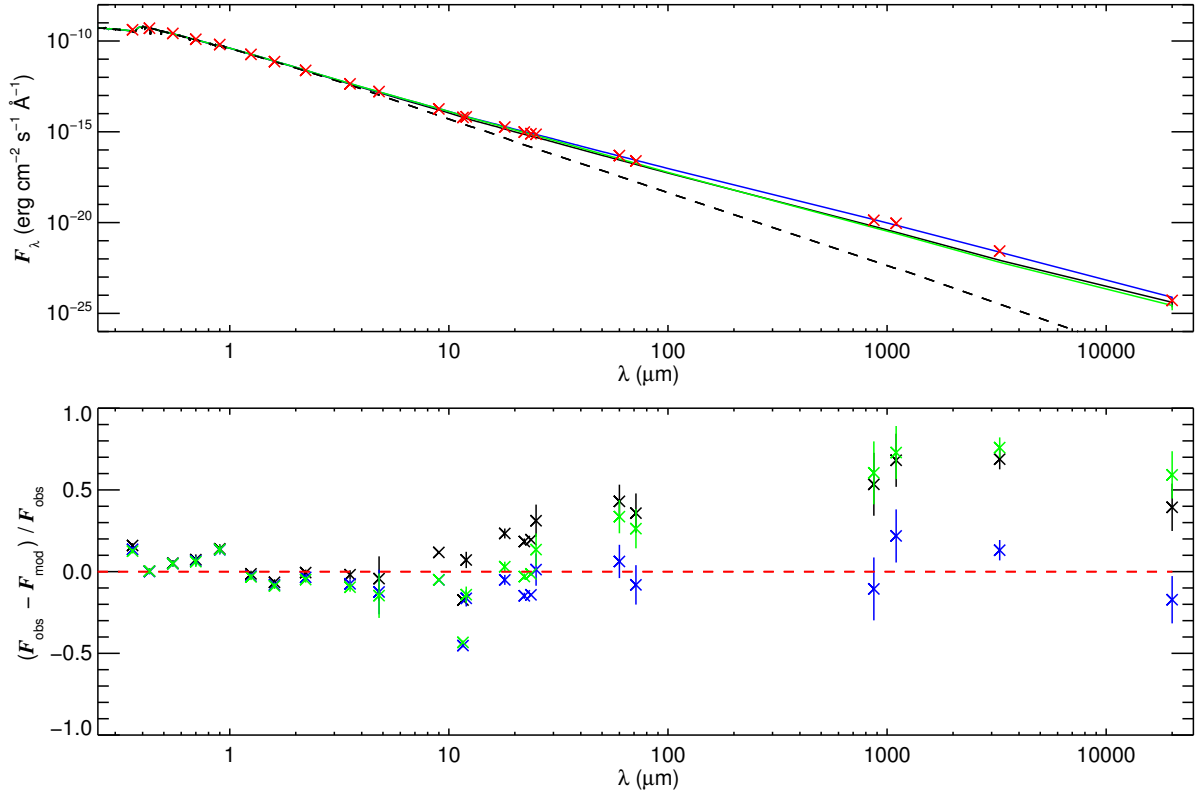runcation and the presence of an unseen binary companion by exploring the outer parts of the disk using the radio data and several unexpected nonhydrogen spectral features.

4.1. SED

4.1.1. UV spectrum

The observed UV spectrum was found to represent the photospheric spectrum of the central star (Fig. 2) almost purely. Therefore the fluxes in the UV region are only influenced by the central star and can be used to constrain its parameters. As M is

kept fixed and β is a known function of W, the parameters that remain to be determined are $R_{\rm p}$, L, and W. While varying L in the interval $160 - 240\,L_\odot$ shifts the flux in the whole UV interval mostly in magnitude, varying $R_{\rm p}$ has a much larger effect on $T_{\rm pole}$ and hence on the spectral slope. With W (and the corresponding β) fixed at the value determined from the analysis of visual polarimetry (Sect. 4.3), and i fixed at the value determined from fitting AMBER interferometry (Sect. 4.4), $R_{\rm p}$ and L can be determined by fitting the UV spectral slope and the UV flux level, respectively. Out of the grid of models computed, the resulting best-fit parameters are $R_{\rm p} = 2.8\,R_\odot$ and $L = 185\,L_\odot$. The model reproduction of the SED structure in the $1000 - 10000$ Å interval is shown in Fig. 3 (as the disk contribution is less than 3%
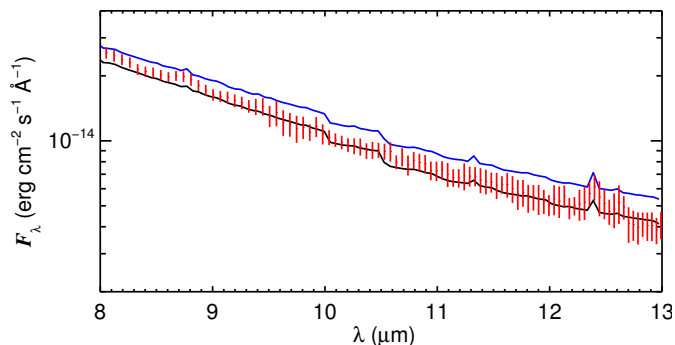
Fig. 5. The parametric model with *n*=3.5 (black) and *n*=3.0 (blue) mid-IR flux predictions compared to the MIDI *N*-band photometry.

in these parts on average, the outcomes of the two VDD model formalisms are identical).

4.1.2. Optical and IR SED

As discussed in the Introduction, the size of the disk pseudophotosphere grows with wavelength. Consequently, the near-IR regions are useful to probe the inner parts of the disk and constrain the disk base density ρ_0, while the SED structure at longer wavelengths traces the density falloff exponent *n*. The resulting ρ_0 from the best-fit parametric model is 2.0×10^{-12} g·cm^{-3}; the implications for *n* in the light of the whole SED structure are discussed below.

The parametric model with a single value of *n* throughout the whole disk does not seem to provide an entirely satisfactory description of the density profile. In Fig. 4 we see that the parametric model with $n = 3.5$ reproduces the SED well only until ∼15 µm, while it underestimates the far-IR and radio fluxes by about 40–70%. A shallower density profile with $n = 3.0$ (and the same ρ_0) reproduces the SED longward of ∼15 µm much better at the expense of the mid-IR fluxes, which become slightly overestimated by about 20%, as may also be seen in Fig 5, which shows the comparison of the parametric model to the *N*-band MIDI photometry.

The self-consistent model SED is very similar to the parametric $n = 3.0$ model at wavelengths up to ∼15 µm, showing only slight effects of nonisothermality in the inner, central parts of the disk, which are consistent with the predictions: The temperature initially decreases, which leads to a shallower radial density profile in the inner parts of the disk (see Fig. 4 of Carciofi & Bjorkman 2008). At longer wavelengths, the self-consistent model approaches the $n = 3.5$ model, as the disk temperature rises and becomes roughly isothermal in its more extended regions.

Overall, we find that neither the parametric model with a single *n*, nor the self-consistent model, are able to perfectly reproduce the observed SED structure, which suggests that the disk has a more complicated density profile than a simple power law, or steady decretion. We discuss the density structure further when we compare the model to the remaining observables, and we return to the issue of nonisothermality in Sect. 4.7.

4.2. The hydrogen emission line profiles

The overall shape, equivalent width, FWHM, and the ratio of maximum to continuum intensity of the observed Hα line profile is in reasonable (with respect to the used methods) agreement with the historic measurements from 1950 to 1991 (Slettebak &
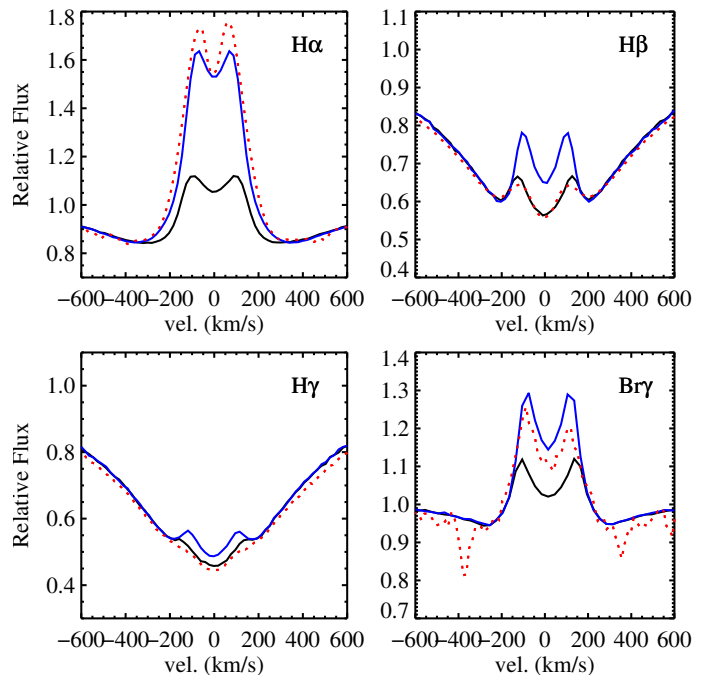

Fig. 6. Hydrogen line profiles for the parametric model (solid lines) with $n = 3.5$ (black) and $n = 3.0$ (blue) compared to the averaged observed hydrogen line profiles (dotted red lines). The self-consistent model (not shown) is almost identical to the $n = 3.5$ parametric model. While Hβ and Hγ are reproduced well with $n = 3.5$, Hα and Brγ need $n = 3.0$ for their emission to reach the observed values.

Reynolds 1978; Slettebak 1982; Andrillat & Fehrenbach 1982; Hanuschik et al. 1996). The hydrogen lines Hα, Hβ, Hγ, and Brγ all show evidence of a double-peaked emission component. Using the best-fit parametric and self-consistent models, we calculated both line profiles and images to provide an additional consistency check of the disk density structure, as the higher Balmer lines originate progressively closer to the star. The line profile results (Fig. 6) clearly show that a model with a single power law describing the radial density falloff is unable to simultaneously fit all four lines. While Hβ and Hγ, which originate in the inner regions of the disk, are reproduced well with $n = 3.5$, Hα and Brγ, which come from much more extended parts of the disk, require $n = 3.0$ to attain the observed level.

The outcome is similar to what was suggested by the SED analysis. A steeper falloff (higher *n*) is needed in the inner parts, where Hβ, Hγ, and near-IR continuum (but also the visual polarization, see the following section) originate, while in the more extended parts, where Hα, Brγ, and far-IR emission come from, a shallower density profile is needed to increase the size of the optically thick emitting area and hence the line equivalent width. This again indicates that a single power law throughout the disk is not a suitable description of the density profile. The outcome of the self-consistent model for these four lines is almost identical to the parametric model with $n = 3.5$.

For very optically thick emission lines, such as Hα, the line photons are absorbed and re-emitted many times within the Sobolev zone before they escape. This diffusion process greatly increases the probability that some fraction of the Hα line photons are scattered by free electrons, which have much larger thermal velocities than the hydrogen lines. To simulate this effect, we thermally broadened a fraction, $f = 0.6$, of the Hα photons by convolving those photons with a Gaussian of width $v_{es} = 300$ km·s^{-1}. The remaining fraction $(1 - f)$ of the Hα photons
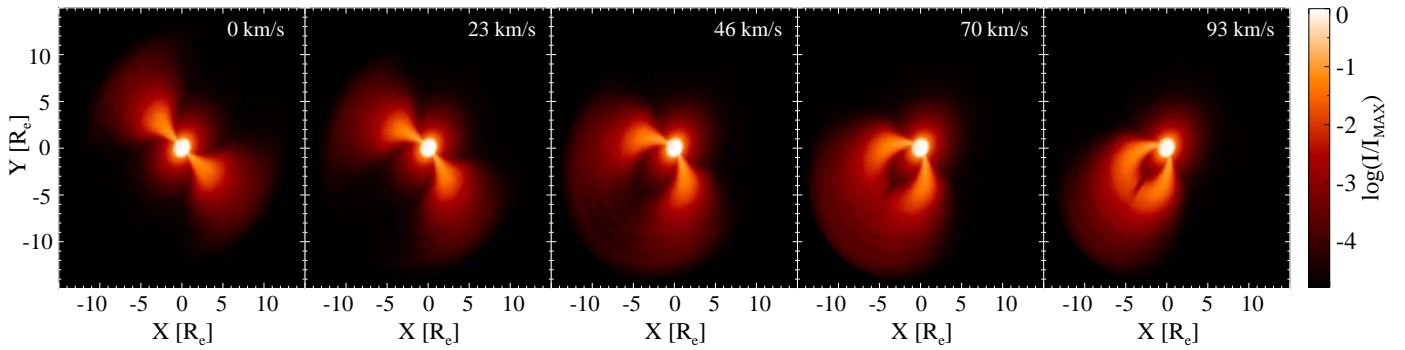
Fig. 9. Synthetic images of the isovelocity regions across the Brγ emission line. The zero velocity corresponds to the line center.
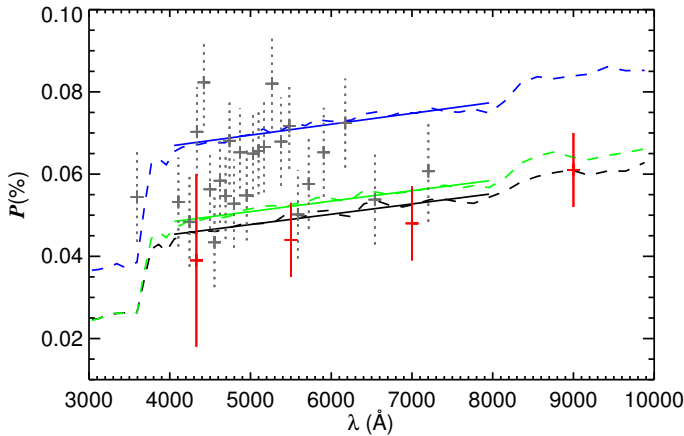

Fig. 7. The spectral shapes of polarization (dashed lines) overplotted with their linear fits (solid lines) in the Paschen continuum: parametric model with $n = 3.5$ (black), parametric model with $n = 3.0$ (blue), and self-consistent model (green). The OPD measurements are plotted in red and for comparison we show the binned 1991 HPOL measurement (gray plus signs with dotted error bars).
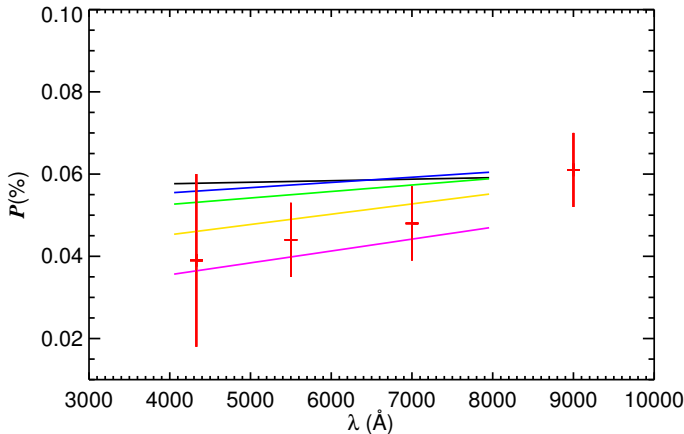

Fig. 8. The influence of W on the model spectral slope in the Paschen continuum for the parametric model with $n = 3.5$. The plotted models are for $W = 0.80$ (black), $W = 0.95$ (blue), $W = 0.97$ (green), $W = 0.99$ (yellow), and $W = 1.0$ (purple). The average of OPD measurements in the *BVRI* filters is plotted in red.

are left unbroadened. The values of f and v_{es} were chosen empirically to best reproduce the wings of the observed Hα profile. The electron thermal velocity at $T_k = 6500$ K is 310 km·s^{-1}, which is roughly what we determined empirically for v_{es}. The

remaining Balmer lines (Hβ, Hγ and Brγ) are much weaker, so we applied no electron scattering broadening to those lines.

4.3. The optical polarization

The HPOL measurements show a level of variability, which is hard to quantify due to their large errors and scarce temporal coverage throughout the years 1990 – 2005. They are consistent though with a very low level of polarization in the range of 0.01 – 0.10%, suggesting no large-scale mass injection or dissipation episodes have occured over the past few decades. The OPD data covering approximately the last four years show a polarization level of ∼0.02 – 0.07% in the *BVRI* Johnson filters, with less scatter compared to the HPOL data and also very little temporal variation (Table 3, available electronically only).

For the modeling purposes, we used the averaged values of the OPD measurements. Despite the uncertainties being quite large, the data clearly show a positive spectral slope of the polarization level in the Paschen continuum (see Fig. 7). This is an unusual feature and is not seen in any of the theoretical polarization spectra shown by Haubois et al. (2014); in that work, low-density models have either flat spectra, indicative of the prevalence of Thomson scattering in the total opacity (i.e., low-density models), or negative slopes for the cases where H opacity contributes significantly to the total opacity (i.e., high-density models). In view of that, we explored which model parameter could be responsible for the positive slope. We used only the Paschen continuum polarization levels to compare the model and observed slopes to avoid the influence of Balmer and Paschen jumps.

Increasing the rotation rate W closer to the critical value was found to be the major factor causing the polarimetric slope to attain the unusual positive slope shown by the observations. The dependence of model polarization on W is shown in Fig. 8. Only rotation rates higher than about 0.90 produce a positive polarimetric slope, while rotation rates higher than $W = 0.98$ are required to reproduce the observations within the error bars. The dependence of the polarimetric slope on the rotation can be probably explained by the fact that the flux constrast between the pole and the equator gets stronger at shorter wavelengths (e.g., Fig. 6 of Rivinius et al. 2013a). Since polarization is the ratio between the scattered to direct startlight, it follows that polarization should be smaller where the flux constrast is the strongest. This effect is only valid for tenuous disks whose dominant opacity (Thomson scattering) is gray. Denser disks attain a negative slope reflecting the strong contribution of H to the total opacity. The finding of such a fast rotation is supported by the results of Saio et al. (2007), who found nonradial pulsation modes (pro-
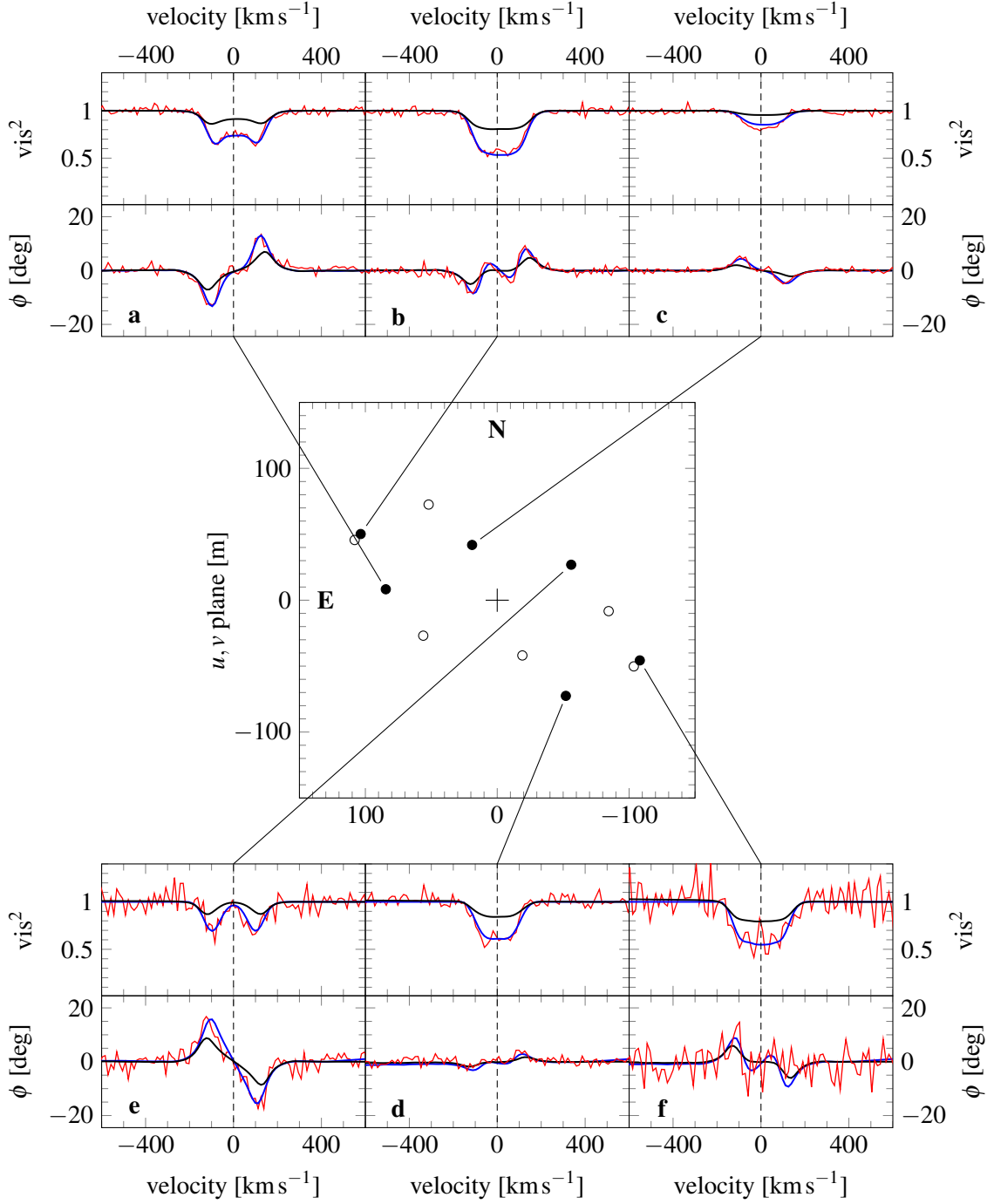
Fig. 10. The parametric model with $n = 3.5$ (black) and $n = 3.0$ (blue) fits to the visibilities and phases measured by AMBER (red). The outcome of the self-consistent model is identical to the $n = 3.5$ parametric model. In the middle panel, the filled circles are the uv-plane positions of the observations, while the open circles are their conjugates.

grade sectoral g-modes of $m = -1$) excited in β CMi, which they only predict to be stable if the star rotates nearly critically.

The predictions of the adopted models with $W = 0.99$, compared to the average of OPD measurements, are shown in Fig. 7. The parametric model with $n = 3.0$ overestimates the polarization level, while using $n = 3.5$ matches the observed level well. This further corroborates what was suggested by the SED and line profile analysis, i.e., a steep density falloff in the inner parts and a shallower profile farther on.

The polarization level is strongly dependent on the inclination angle i with the maximum level observed when $i \sim 70-80°$

(Halonen & Jones 2013). However, the inclination was found to be well constrained by the AMBER data (see Sect. 4.4), which allows us to use the polarization level to constrain the density structure of the inner disk without a degeneracy with respect to i.

4.4. AMBER spectrointerferometry

AMBER data allow us to study the geometry and extension of the Brγ emitting region. To accomplish this, we calculated the synthetic Brγ images (several shown in Fig. 9) across the emis-
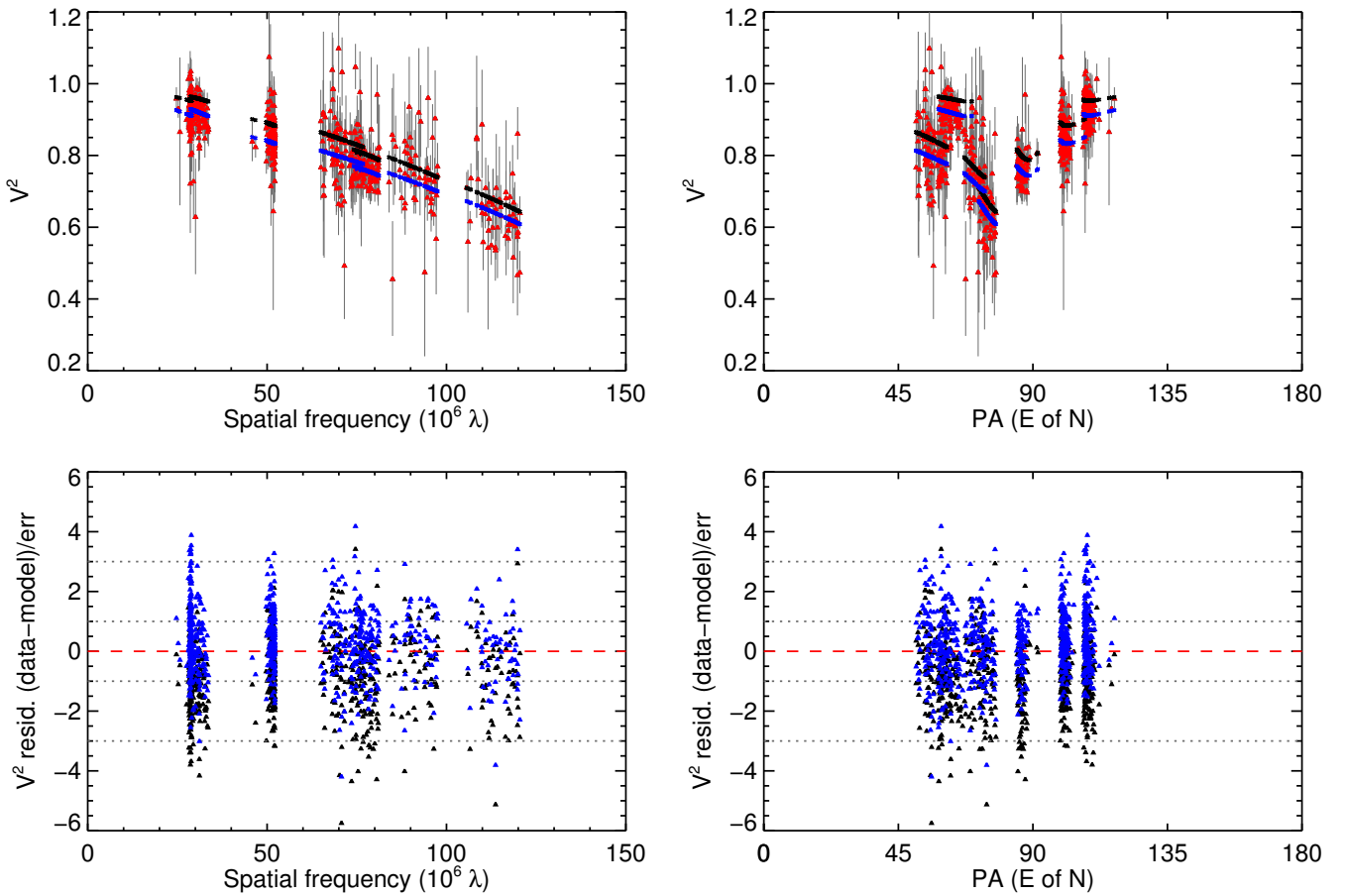
Fig. 11. The NPOI Hα channel squared visibilities (red with gray error bars) overplotted with the corresponding parametric, $n = 3.5$, (black), and $n = 3.0$ (blue) model predictions (compare with the upper left panel of Fig. 6)

sion lines, depicting the corresponding isovelocity regions. From these images we determined the predicted AMBER visibilities and phase shifts across the Brγ line. AMBER's high spectral resolution reveals the spectrointerferometric signatures in the differential visibilities and phases that are expected for circumstellar disks. As was reported by Kraus et al. (2012), and discussed theoretically by Faes et al. (2013), phase reversals occur in the differential phase signatures of β CMi across the Brγ line. Using the terminology of Faes et al. (2013), the disk of β CMi was observed outside the astrometric regime, which means that the ratio between the baseline length and the distance to the star exceeds 1.5 m·pc^{-1}. Thus the differential phases are no longer proportional to photocenter displacement and phase signatures are more complicated than simple S-shaped profiles usually observed for marginally resolved disks.

Similar to the observables believed to originate in the more extended parts of the disk, a shallower density profile with $n = 3.0$ is needed to reproduce the AMBER observations, while the predictions of the $n = 3.5$ parametric model and the self-consistent model are almost identical, clearly underestimating the size of the line emitting region (Fig. 10). The fit of the $n = 3.0$ parametric model to the two sets of AMBER data is remarkable, with a reduced $\chi^2 = 1.20$. This kind of good agreement again implies that the disk velocities are Keplerian, which is strong support for the VDD model. The inclination is well constrained by the shape implied by the visibility data along the various baseline orientations with the best-fit value being $i = 43^{+3°}_{-2°}$. The position angle, *PA*, of the disk major axis projected on the sky was found to be $133^{+4°}_{-3°}$ (from north to east) in a reasonable agreement with the value of $140.0 \pm 1.7°$ found by Kraus et al. (2012). The average polarization position angle from the HPOL synthetic *UBVRI* filter data and OPD measurements is $41.6 \pm 1.8°$ and $50.0 \pm 17.8°$, respectively, in a good agreement with the interferometric *PA*, as the polarization direction is usually perpendicular to the disk major axis, but small variations can be expected from the disk asymmetries responsible for the V/R variations.

4.5. NPOI interferometry

The NPOI data, which contain the Hα line emission in its 15 nm-wide channel, provide an important consistency check of the modeling of the Hα line profile, which could only be reasonably reproduced with a shallow, $n = 3.0$, radial density falloff. Indeed, the NPOI visibilities are better reproduced with the $n = 3.0$ model ($\chi^2 = 1.40$), revealing a larger Hα emitting region than expected from the $n = 3.5$ model ($\chi^2 = 2.08$). The predictions of the two models are compared with the data in Fig. 11. We used an average angular radius of the central star to calibrate all the *PA*s, while the proper approach would be to use the exactly corresponding angular radii to calibrate the individual *PA*s. However, we expect that this would bring only minor improvement of the overall good fit.
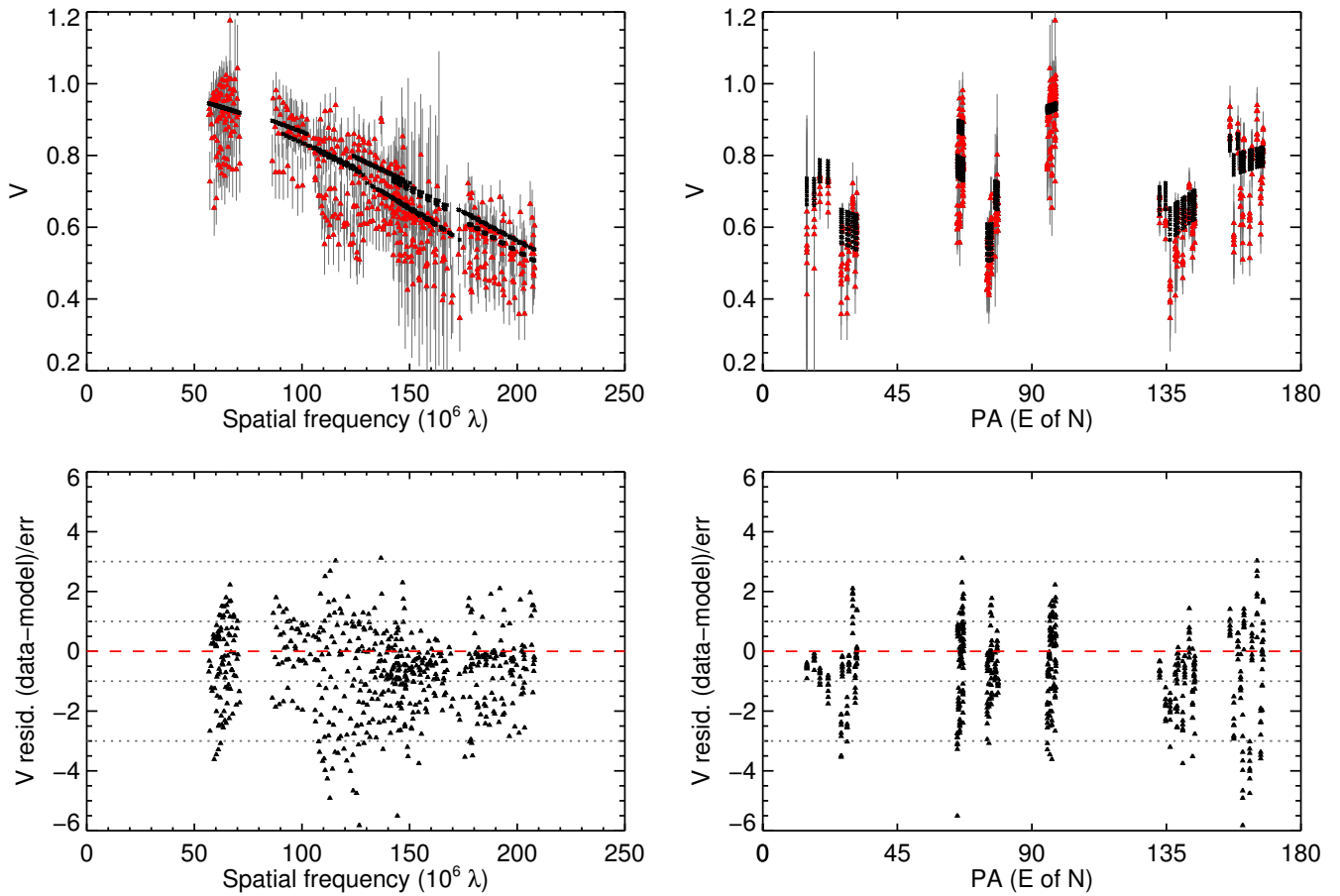
Fig. 13. The MIRC *H*-band visibilities (red with gray error bars) and the corresponding parametric (*n* = 3.5) model predictions (black).

Table 9. Model fits to the interferometric measurements.

Instrument	Spectral band	χ^2 (*n* = 3.5)	χ^2 (*n* = 3.0)
NPOI	*R* (Hα)	2.08	1.40
MIRC	*H*	2.27	2.08
FSU-A	*K*	0.84	0.91
AMBER	*K* (Brγ)	3.90	1.20
CLIMB	*K'*	1.58	1.45
MIDI	*N*	1.80	1.91

Notes. AMBER and NPOI, for which extended line emission plays a major role, are clearly better reproduced by the *n* = 3.0 model. The MIDI, CLIMB, and MIRC data, for which we would expect a better fit by the *n* = 3.5 model, are also slightly better reproduced by the *n* = 3.0 model, but not much weight should be put on these results given the overall low quality of the respective data.

4.6. FSU-A, MIDI, PIONIER, and CHARA interferometry

The remaining interferometric measurements are either very scarce in their *uv*-plane coverage or too noisy to provide a reliable consistency checks of the best-fit model parameters. Nevertheless, the model reproduces these data reasonably well (Table 9).

4.6.1. VLTI

The fit to the three FSU-A *K*-band visibilities is shown in Fig. 12 (available electronically only). The MIDI data covering the *N*-

band spectral region are consistent with an unresolved disk, i.e., values of visibilities ~1 within 1–2σ in a good agreement with both the *n* = 3.5 and *n* = 3.0 parametric models (figure not shown). The only usable outcome of the PIONIER observations was a closure phase measurement consistent with zero ($\pm$ 1.5°), which eliminates any companion up to 5% flux contrast in the 1.5-50 mas separation range.

4.6.2. CHARA

Despite the MIRC data having the best *uv*-plane coverage and the longest projected baselines of all the interferometric measurements presented, significant scatter of the data, often of measurements taken during the same night for almost identical baselines prevented the data from being of much use (Fig. 13). The cloud of residuals is not centered on zero, but below, i.e., the observations often show a lower fringe contrast than predicted. Diminished fringe contrast could be explained by observing issues and/or weather conditions that were not accounted for.

Finally, the model comparison to the *K'*-band CLIMB data is plotted in Fig. 14 (available electronically only).

4.7. Nonisothermal effects on the observables

So far, we have mostly focused on presenting the results of the parametric model as it allows us to test alternative density profiles. In this section, we compare the outcomes of the parametric model with *n* = 3.5 and the self-consistent model and discuss the nonisothermal effects on both the disk structure and model ob-
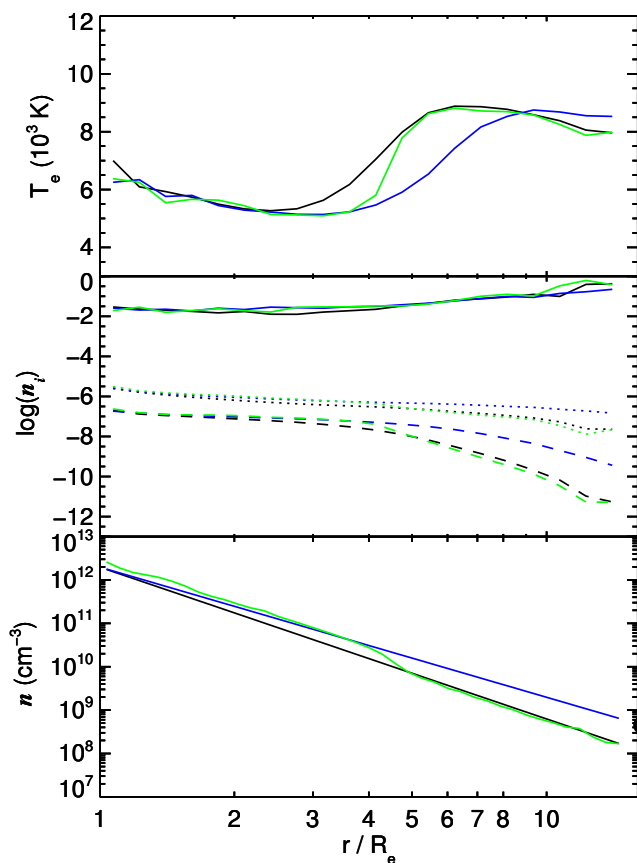
Fig. 15. Electron temperature (T_e), hydrogen level populations (log(n_i)), and number density (n) structures along the disk midplane of the parametric model with $n = 3.5$ (black), $n = 3.0$ (blue) and the self-consistent (green) model. The middle panel contains the n_1 (solid), n_2 (dotted), and n_3 (dashed) level populations.

Fig. 16. *Upper*: sub-mm to cm SED structure of the parametric model ($n = 3.0$). The red crosses correspond to the observed fluxes from APEX (870 μm), JCMT (1.1 mm), CARMA (3.265 mm), and VLA (2 cm). The plotted parametric model (with $n = 3.0$) SEDs (black solid lines) are for $R_{out}/R_e = 10$; 20; 25; 30; 35; 40; 45; 50; 60; 70; 80; 90; and 100 from bottom to top. *Lower*: reduced χ^2 dependence on R_{out} for APEX (solid), CARMA (dotted) and VLA (dashed). The combined χ^2 for all four observations is plotted as a red solid line.

servables that arise when the density structure is self-consistently calculated together with the temperature structure.

The temperature, level populations, and density structures of the two models along the disk midplane are plotted in Fig. 15. The temperature is found to decrease up to about 3 R_e, then to steeply rise, and from about 5 R_e further the disk becomes isothermal and almost neutral. Introducing the self-consistent solution leads to a slight compression of the disk in the vertical direction, while the radial density structure changes as expected from the temperature structure, i.e., the falloff is shallower where the temperature gradient is negative and steeper where the temperature gradient is positive (Carciofi & Bjorkman 2008). This has an effect on the near-IR SED structure, as shown in Fig. 4, and also on the polarization level, which slightly increases because of enhanced density in the inner parts.

The effect of the self-consistent solution on the density structure and SED is opposite to what was inferred from the SED and spectral line analysis, a steep density falloff followed by a shallower falloff. This appears to indicate that some mechanism, other than nonisothermality, is modifying the disk structure. Note, however, that the non-isothermal effects on the observables are small, as expected for a low-density disk around a late-type B star (Carciofi & Bjorkman 2008). The presence of a possible unseen binary companion would most likely have stronger effects on the disk structure, and would prevent us from

finding a global improvement of the model fit to the observations when making the model fully self-consistent.

It is also interesting to note that the model Brγ visibilities and phases are identical for the parametric model with $n = 3.5$ and the self-consistent model, which means that while the density structure changes locally, the outcome for the whole Brγ-emitting region for these two models is the same. We next turn to the evidence in our data for the presence of an unseen binary companion.

4.8. Estimating the disk size from radio fluxes

Contrary to the near-IR, which probes the inner disk, the radio fluxes probe the outermost reaches of the disk. For an isolated disk, the disk can grow to the photoevaporation radius. However, if the disk is physically truncated by a binary, the pseudophotosphere effective radius eventually reaches the disk physical size and the disk flux excess no longer increases with wavelength. Consequently, the SED presents an inflection at the wavelength where $R_\lambda \approx R_{out}$, and follows the photospheric spectral slope at longer wavelengths (see Fig. 11 of Vieira et al. 2015, submitted, for an illustration). Therefore, the observation of this kind of transition in the SED slope can place important constraints on the disk physical size.

Under the assumption that the shallower density profile needed to reproduce the mid- to far-IR SED structure also holds throughout the radio emitting region, we tested which disk radii reproduce best the mm and cm SED structure. In the upper panel of Fig. 16, we plot the sub-mm to cm SED for models with different R_{out} and, in the lower panel, the corresponding reduced χ^2. The APEX and JCMT fluxes are already reproduced for R_{out}
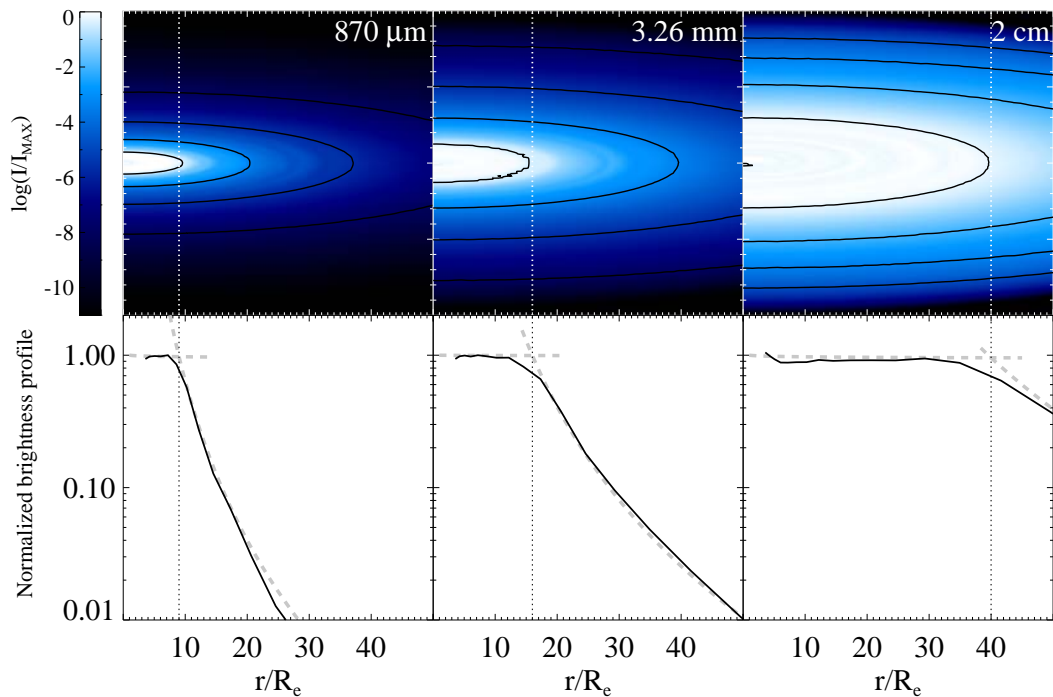
Fig. 17. Synthetic images computed with HDUST (upper panels) and their respective radial brightness profile curves (lower panels), at $870\,\mu$m, 3.26 mm, and 2 cm. In all cases, the maximum disk emission was normalized to unity. Overplotted to the images are the contours of same flux, at $\log(I/I_{\text{MAX}}) = -0.2$, -1.5, -2.5, and -3.5 (which correspond to 63%, 3%, 0.3%, and 0.003% of the disk maximum brightness, respectively). The transition between the optically thick region (pseudophotosphere) and the diffuse part of the disk is indicated by a vertical dotted line over the plots, as estimated from the extrapolation of the distinct brightness profile regions (gray dashed curves).

$= 20\,R_{\text{e}}$ and increasing R_{out} beyond this value does not lead to further enhancement of the model flux. The physical explanation for this is that the size of the pseudophotosphere at these wavelengths is about 10-20 R_{e}, so increasing the disk size beyond this value does not result in an increase in the disk emission. The behavior at CARMA wavelength is similar, but R_{out} of at least $40\,R_{\text{e}}$ is needed. At 2 cm, however, the situation is different. While the lowest residual between the model and observed flux is seen for $R_{\text{out}} = 35\,R_{\text{e}}$, a higher value of R_{out} overestimates the observed flux. The best-fit value of R_{out} is found to be $35^{+10}_{-5}\,R_{\text{e}}$.

In Fig. 17 we show the synthetic images and graphical representation of the brightness profiles at wavelengths corresponding to the APEX, CARMA, and VLA observations with the estimates of the corresponding pseudophotosphere sizes. Indeed, as expected from the model behavior, at the shorter wavelengths $\bar{R}_\lambda$ is between 10–20 R_{e}. However, $\bar{R}_\lambda$ at 2 cm is about 40 R_{e}, thus larger than the estimated disk size. The 2 cm results can therefore be interpreted as a clear sign of truncation by an unseen binary companion, however, this conclusion rests on the reliability of a single non-contemporaneous data point.

4.9. Spectral features of other elements

To explore the additional spectral features in the interval covered by the FEROS and ESPaDOnS spectra, we used an updated version of the BRUCE3 code (see Rivinius et al. 2013b, and the references therein) to compute a purely photospheric, high-resolution spectrum for the stellar parameters listed in Table 7.

An unusual feature is present in both the FEROS and ESPaDOnS spectra. The calcium triplet (CaII λ8498, 8542, and 8662 Å) is in emission (blended with the Paschen lines Pa16, Pa15, and Pa13), but is noticeably stronger than the emission

from the unblended Paschen line Pa14 (Fig. 18). This effect was linked to possible binarity of Be stars by Polidan (1976), while a correlation of the presence of this feature in a number of B subdwarf (sdB) stars with a cool companion was reported by Jeffery & Pollacco (1998). The emission in this case probably originates in the very outer disk, which is possibly partially accreting onto the secondary component.

Moreover, in the CaII λ3934 line, the emission component is noticeably narrower than the absorption component (left panel of Fig. 19), while the opposite is expected for a line originating in the fast-rotating inner disk. Therefore, similarly to the calcium triplet mentioned above, the emission seems to actually originate in the outer disk, close to a possible secondary companion.

Finally, the ultraviolet CIV λ1548 line exhibits a P Cygni profile with a blue edge velocity of $\sim$230 km·s^{-1} (right panel of Fig. 19), which is a clear signature of a fast stellar wind. The presence of this line is not expected in this late-type B star (see Fig. 11 of Rivinius et al. 2013a). Additionally, the observed velocity is lower than is typical for late B stars. This suggests that this kind of wind might be excited by the radiation of a companion, which interacts with the outer disk of the primary Be star.

5. Discussion on the possible binarity

Using the radio flux measurement at the wavelength of 2 cm in combination with a well-sampled SED at shorter wavelengths, we found observational evidence suggesting truncation of the disk of β CMi at about 35 R_{e}. The most probable mechanism that can truncate the disk at this radius is the tidal influence of an orbiting binary companion. The presence of an unseen binary companion is also suggested by weak V/R oscillations of the Hα line and the appearance of the CaII λ3934 emission line and the triplet CaII λ8498, 8542, 8662. Additionally, the CIV λ1548
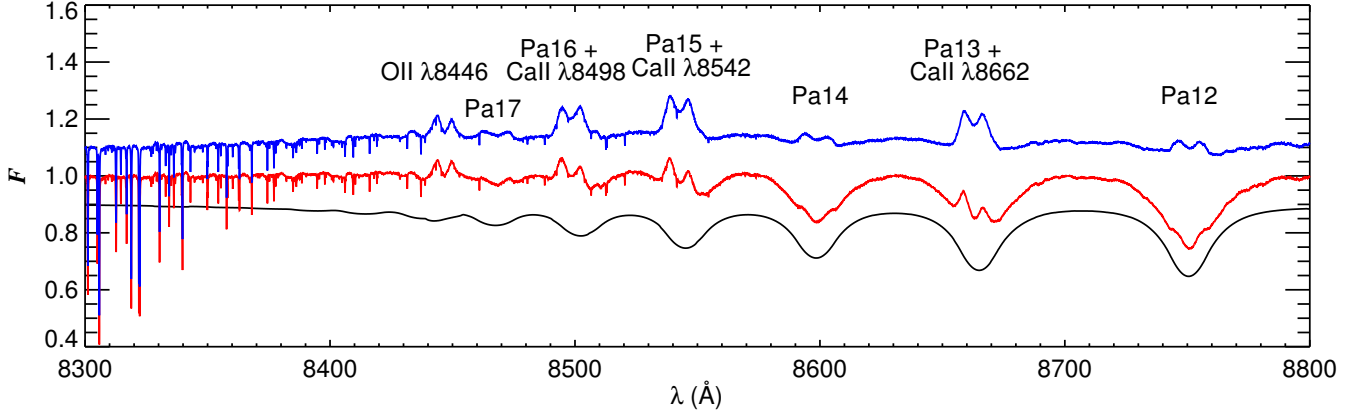
Fig. 18. Ca triplet spectral feature. The BRUCE model photospheric spectrum (black) is plotted alongside the averaged normalized spectrum observed by ESPaDOnS (red) and the difference between the two, which represents the pure emission component (blue). Both the observed and pure emission spectrum show that the Paschen lines Pa16, Pa15, and Pa13 blended with calcium emission CaII λ8498, 8542, and 8662, respectively, are much stronger than the emission from the unblended Paschen lines.
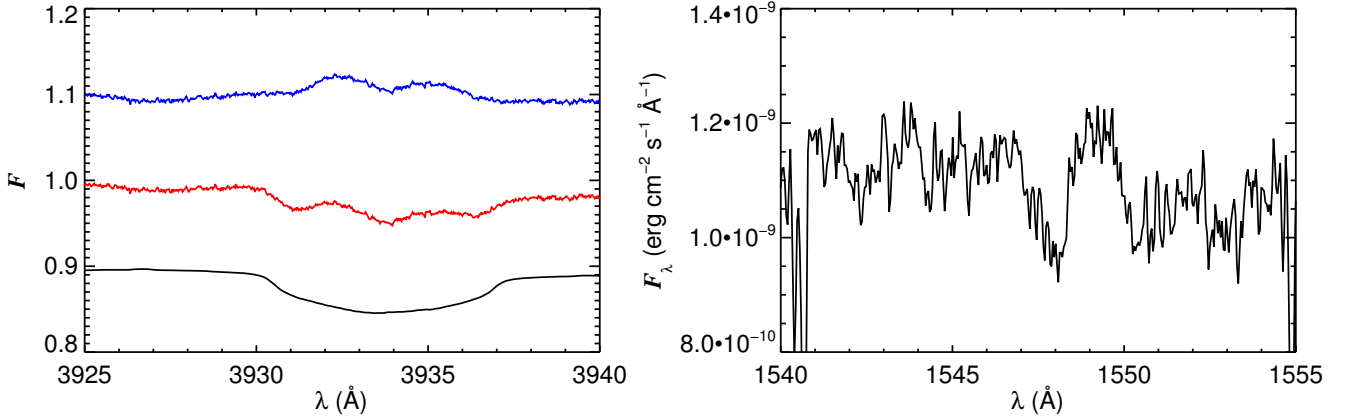
Fig. 19. *Left:* CaII λ3934 line. The purely photospheric model absorption (black) is plotted alongside the normalized ESPaDOnS spectrum (red) and their difference is plotted in blue. The emission component is clearly narrower than the absorption. *Right:* CIV λ1548 line as observed by IUE showing a clear P Cygni profile.

line sugggests a hot, possibly subdwarf (sdB or sdO) companion. The proposed companion has to be faint, as its signatures are seen neither in the spectra nor in the SED. The detection limits from interferometric measurements set the spectral type of a main-sequence companion to be F5 or later, thus putting an upper limit of $\sim$0.5 on the mass ratio q.

To test whether a binary companion could truncate the disk at the radius estimated from the modeling, we made the assumption that the V/R variations in Hα are indeed caused by a companion, in which case the period of these oscillations ($\sim$183 days, Folsom et al. 2015) can be used as an estimate of the orbital period. We then performed simulations of the binary system in a circular orbit with a smoothed particles hydrodynamics (SPH) code (Okazaki et al. 2002), which assumes an isothermal disk, to determine the truncation radius, R_t, resulting from the presence of the possible companion. In the SPH simulation, the Be star disk is initially nonexistent. We then assume a constant mass injection rate from the equator of the star onto the equatorial plane, so that after letting the system evolve, we achieve a base density ρ_0 equal to its constrained value (Table 7) . We explored the outcome of those simulations (shown in Fig. 20) for different viscosity parameters, $\alpha \in \{0.1, 1.0\}$, and mass ra-

tios, $q \in \{0.1, 0.5\}$. Figure 20 shows the surface density structure of representative models after a long period of disk evolution (30 orbital periods) to ensure that the disk has reached a quasi-steady-state configuration (Panoglou et al. 2015; Haubois et al. 2012). Following Okazaki et al. (2002), the truncation radius is estimated by fitting the expression

$$\Sigma = A \frac{(r/R_t)^{-k}}{1 + (r/R_t)^l} \tag{6}$$

to the results of the SPH simulations, where A, R_t, k, l are constants to be fit. The resulting truncation radii range from $\sim$18 R_e ($\alpha = 0.1$; $q = 0.5$) to $\sim$25 R_e ($\alpha = 0.1$; $q = 0.1$), as compared to an R_{out} of 35^{+10}_{-5} R_e determined from the SED fitting. A certain discrepancy is to be expected because in the HDUST model, the disk is entirely cut off at $\sim$35 R_e. In contrast, the truncation radius in the SPH simulations represents a point were the density falloff becomes steeper (Fig. 20), but the disk still exists beyond this point. This means that the size of the pseudophotosphere at 2 cm should in principle be somewhat larger than R_t, which would reconcile the two results.

Out of the explored mass ratios and viscosity parameters, the $q = 0.5$ and $\alpha = 0.1$ simulation is the only one that clearly causes
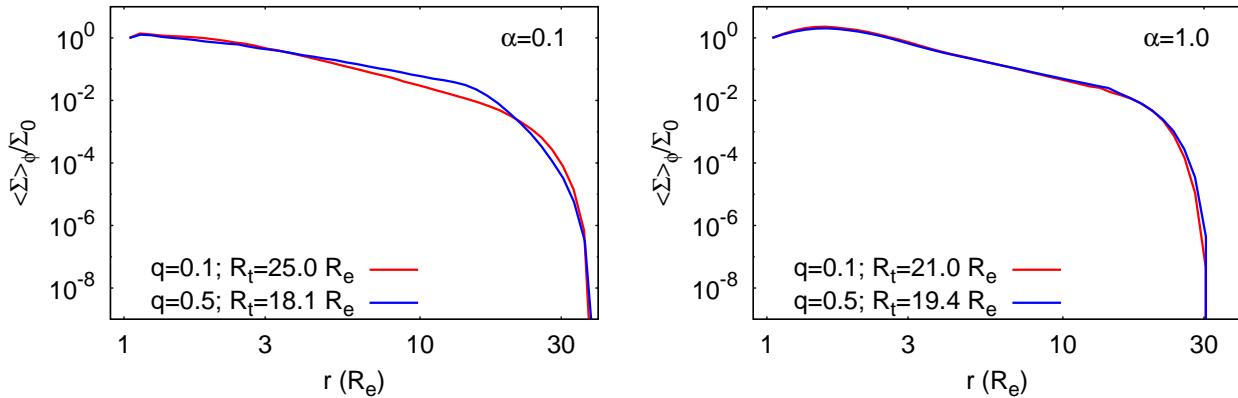
Fig. 20. Results of the SPH simulations showing density profiles of isothermal disks influenced by the assumed binary companion in a circular orbit with $P = 182.83$ days, and different mass ratios, as indicated. *Left*: simulations for viscosity parameter $\alpha = 0.1$. *Right*: simulations for $\alpha = 1$. What is plotted is the azimuthally averaged surface density after 30 orbital periods. The truncation occurs where the density slope changes to a much steeper slope.

the density structure of the disk inward of R_t to attain a shallower profile of $n = 3.0$, which is the value that was determined for intermediate part of the disk (inward of R_{out}) from the HDUST modeling. However, the steeper density profile in the very inner parts of the disk is not reproduced by the simulation, although there is a possibility that the introduction of nonisothermality into the SPH simulation might show the desired effect.

In any case, although the proposed binarity is quite probable, this must be viewed with caution. Firstly, the evidence for the disk truncation is based only on one single measurement from more than 30 years ago. Despite the apparent stability of the disk over the last ~15 years, as shown by our spectroscopic data set, and an overall stability over the last ~65 years according to the literature, we cannot exclude the possibility that the mass injection rate into the disk has changed over the last decades to a degree that would destroy evidence of truncation. Secondly, it is unclear whether the complicated density structure including the inner parts is compatible with the presence of the binary companion, although the tidal interaction seems to offer the most straightforward explanation. A careful analysis of nonisothermal SPH simulations is necessary to explore if the presence of the companion offers the explanation, or if other causes are needed. Since this is beyond the scope of the present analysis, we plan to return to this issue in a follow-up paper. In that paper, we intend to study the density profile in more detail as well as execute our own analysis of the V/R oscillations using all available measurements of Hα and possibly other emission lines.

In addition to binarity, possible mechanisms for truncating the disk are photoevaporation by gas pressure and line driven radiative ablation (Feldmeier et al. 1999; Gayley et al. 1999). The former was already examined in Sect. 3.2 and affects the disk structure only at very large radii. The latter, however, is a possibility to consider. Using the stellar wind mass-loss rate estimate of Castor et al. (1975), Krtička et al. (2011) have determined that the disk wind mass-loss rate scales with the stellar wind mass-loss rate, but with values lower by more than an order of magnitude. This implies that the disk ablation produces a mass loss much lower than that of a main-sequence star. As the winds of late-type main-sequence B stars are typically weak, we conclude that for stars, such as β CMi, wind ablation should not play a role in the truncation of the disk.

6. Conclusions

We tested the ability of the VDD model to reproduce arguably the largest data set of multiwavelength and multitechnique observations of a Be star (β CMi), including the SED covering five orders of magnitude in wavelength, emission line profiles of four hydrogen lines, visual polarimetry, high-resolution, near-IR spectrointerferometry and visual, near-IR, and mid-IR broadband interferometry. Neither a single power-law structure nor steady viscous decretion appears to be an entirely adequate description of the density profile. Observables originating in the inner disk (polarization, higher Balmer lines, near-IR photometry) require the steeper radial power-law exponent $n = 3.5$, while observables originating from more extended regions (Hα, Brγ, mid- to far- IR photometry, sub-mm/mm photometry) require the shallower $n = 3.0$. It is shown that nonisothermal effects on the disk structure cannot account for this more complicated density behavior. Instead, an outer tidal influence most probably exerted by an unseen binary companion is needed, which remains a possibility to be investigated in detail in the future.

Analysis of radio observations suggests truncation of the disk at the distance of 35^{+10}_{-5} R_e from the star. This value was compared with the truncation radius exerted by a possible binary companion with the orbital period corresponding to the period of weak V/R oscillations of the Hα line with an overall good agreement. Together with spectroscopic evidence and a nondetection by any of the other observations, either a late (F5 or later) main-sequence companion or a subdwarf (sdB or sdO) companion is favored.

We report on the diagnostic potential of the polarimetric slope in the Paschen continuum for constraining the rotation rate W. The observed positive slope could only be reproduced with rotation rates very close to critical, with a favored value of $W \gtrsim 0.98$. The almost purely photospheric UV spectrum allowed us to constrain the polar radius $R_p = 2.8$ $R_\odot$ and luminosity $L = 185$ $L_\odot$ of the central star. Finally, AMBER spectrointerferometry facilitated a precise estimation of the inclination angle ($i = 43^{+3°}_{-2°}$). Therefore, to conclude, these results underscore the utility of multitechnique and multiwavelength observations to constrain the disk structure unambiguously, as well as the use of radio observations to study the properties of the outer parts of Be disks.

References

Abt, H. A., Levato, H., & Grosso, M. 2002, ApJ, 573, 359
Andrillat, Y. & Fehrenbach, C. 1982, A&AS, 48, 93
Armstrong, J. T., Mozurkewich, D., Rickard, L. J., et al. 1998, ApJ, 496, 550
Bjorkman, J. E. 1997, in Lecture Notes in Physics, Berlin Springer Verlag, Vol. 497, Stellar Atmospheres: Theory and Observations, ed. J. P. De Greve, R. Blomme, & H. Hensberge, 239
Bjorkman, J. E. 2012, in Astronomical Society of the Pacific Conference Series, Vol. 464, Circumstellar Dynamics at High Resolution, ed. A. C. Carciofi & T. Rivinius, 85
Bjorkman, J. E. & Carciofi, A. C. 2005, in Astronomical Society of the Pacific Conference Series, Vol. 337, The Nature and Evolution of Disks Around Hot Stars, ed. R. Ignace & K. G. Gayley, 75
Bock, D. C.-J., Bolatto, A. D., Hawkins, D. W., et al. 2006, in Society of Photo-Optical Instrumentation Engineers (SPIE) Conference Series, Vol. 6267, Society of Photo-Optical Instrumentation Engineers (SPIE) Conference Series, 13
Carciofi, A. C. 2011, in IAU Symposium, Vol. 272, IAU Symposium, ed. C. Neiner, G. Wade, G. Meynet, & G. Peters, 325–336
Carciofi, A. C. & Bjorkman, J. E. 2006, ApJ, 639, 1081
Carciofi, A. C. & Bjorkman, J. E. 2008, ApJ, 684, 1374
Carciofi, A. C., Bjorkman, J. E., Otero, S. A., et al. 2012, ApJ, 744, L15
Carciofi, A. C., Magalhães, A. M., Leister, N. V., Bjorkman, J. E., & Levenhagen, R. S. 2007, ApJ, 671, L49
Carciofi, A. C., Miroshnichenko, A. S., Kusakin, A. V., et al. 2006, ApJ, 652, 1617
Carciofi, A. C., Okazaki, A. T., Le Bouquin, J.-B., et al. 2009, A&A, 504, 915
Cardelli, J. A., Clayton, G. C., & Mathis, J. S. 1989, ApJ, 345, 245
Castor, J. I., Abbott, D. C., & Klein, R. I. 1975, ApJ, 195, 157
Chelli, A., Utrera, O. H., & Duvert, G. 2009, A&A, 502, 705
Coté, J. & Waters, L. B. F. M. 1987, A&A, 176, 93
Cutri, R. M. & et al. 2014, VizieR Online Data Catalog, 2328, 0
Domiciano de Souza, A., Kervella, P., Moser Faes, D., et al. 2014, A&A, 569, A10
Dougherty, S. M., Taylor, A. R., & Clark, T. A. 1991a, AJ, 102, 1753
Dougherty, S. M., Taylor, A. R., & Waters, L. B. F. M. 1991b, A&A, 248, 175
Dougherty, S. M., Waters, L. B. F. M., Burki, G., et al. 1994, A&A, 290, 609
Ducati, J. R. 2002, VizieR Online Data Catalog, 2237, 0
Espinosa Lara, F. & Rieutord, M. 2011, A&A, 533, A43
Faes, D. M., Carciofi, A. C., Rivinius, T., et al. 2013, A&A, 555, A76
Feldmeier, A., Shlosman, I., & Vitello, P. 1999, ApJ, 526, 357
Folsom, L., Miroshnichenko, A. S., Danford, S., Zharikov, S. V., & Sawicki, C. J. 2015, in Bright Emissaries: Be Stars as Messengers of Star-Disk Physics, in press, ed. A. Sigut & C. Jones, Astronomical Society of the Pacific Conference Series

Gayley, K. G., Owocki, S. P., & Cranmer, S. R. 1999, ApJ, 513, 442
Halonen, R. J. & Jones, C. E. 2013, ApJ, 765, 17
Hanuschik, R. W., Hummel, W., Sutorius, E., Dietle, O., & Thimm, G. 1996, A&AS, 116, 309
Haubois, X., Carciofi, A. C., Rivinius, T., Okazaki, A. T., & Bjorkman, J. E. 2012, ApJ, 756, 156
Haubois, X., Mota, B. C., Carciofi, A. C., et al. 2014, ApJ, 785, 12
Hummel, C. A., Benson, J. A., Hutter, D. J., et al. 2003, AJ, 125, 2630
Hummel, C. A., Mozurkewich, D., Armstrong, J. T., et al. 1998, AJ, 116, 2536
Ishihara, D., Onaka, T., Kataza, H., et al. 2010, A&A, 514, A1
Jarad, M. M., Hilditch, R. W., & Skillen, I. 1989, MNRAS, 238, 1085
Jeffery, C. S. & Pollacco, D. L. 1998, MNRAS, 298, 179
Jones, C. E., Tycner, C., Sigut, T. A. A., Benson, J. A., & Hutter, D. J. 2008, ApJ, 687, 598
Kaufer, A., Stahl, O., Tubbesing, S., et al. 1999, The Messenger, 95, 8
Kovács, A. 2008, in Society of Photo-Optical Instrumentation Engineers (SPIE) Conference Series, Vol. 7020, Society of Photo-Optical Instrumentation Engineers (SPIE) Conference Series, 1
Kraus, S., Monnier, J. D., Che, X., et al. 2012, ApJ, 744, 19
Krtička, J., Owocki, S. P., & Meynet, G. 2011, A&A, 527, A84
Kurucz, R. L. 1979, ApJS, 40, 1
Le Bouquin, J.-B., Berger, J.-P., Lazareff, B., et al. 2011, A&A, 535, A67
Lee, U., Osaki, Y., & Saio, H. 1991, MNRAS, 250, 432
Leinert, C., Graser, U., Przygodda, F., et al. 2003, Ap&SS, 286, 73
Meilland, A., Stee, P., Chesneau, O., & Jones, C. 2009, A&A, 505, 687
Meilland, A., Stee, P., Vannier, M., et al. 2007, A&A, 464, 59
Monnier, J. D., Pedretti, E., Thureau, N., et al. 2006, in Society of Photo-Optical Instrumentation Engineers (SPIE) Conference Series, Vol. 6268, Society of Photo-Optical Instrumentation Engineers (SPIE) Conference Series, 1
Müller, A., Pott, J.-U., Mérand, A., et al. 2014, A&A, 567, A98
O'Donnell, J. E. 1994, ApJ, 422, 158
Okazaki, A. T. 2001, PASJ, 53, 119
Okazaki, A. T., Bate, M. R., Ogilvie, G. I., & Pringle, J. E. 2002, MNRAS, 337, 967
Panoglou, D., Carciofi, A. C., Okazaki, A., & Rivinius, T. 2015, in Bright Emissaries: Be Stars as Messengers of Star-Disk Physics, in press, ed. A. Sigut & C. Jones, Astronomical Society of the Pacific Conference Series
Petrov, R. G., Malbet, F., Weigelt, G., et al. 2007, A&A, 464, 1
Polidan, R. S. 1976, in IAU Symposium, Vol. 70, Be and Shell Stars, ed. A. Slettebak, 401
Porter, J. M. 1999, A&A, 348, 512
Rivinius, T., Carciofi, A. C., & Martayan, C. 2013a, A&A Rev., 21, 69
Rivinius, T., Townsend, R. H. D., Kochukhov, O., et al. 2013b, MNRAS, 429, 177
Sahlmann, J., Ménardi, S., Abuter, R., et al. 2009, A&A, 507, 1739
Saio, H., Cameron, C., Kuschnig, R., et al. 2007, ApJ, 654, 544
Secchi, A. 1866, Astronomische Nachrichten, 68, 63
Sigut, T. A. A. & Jones, C. E. 2007, ApJ, 668, 481
Silaj, J., Jones, C. E., Tycner, C., Sigut, T. A. A., & Smith, A. D. 2010, ApJS, 187, 228
Siringo, G., Kreysa, E., Kovács, A., et al. 2009, A&A, 497, 945
Slettebak, A. 1982, ApJS, 50, 55
Slettebak, A. & Reynolds, R. C. 1978, ApJS, 38, 205
Struve, O. 1931, ApJ, 73, 94
Sturmann, J., ten Brummelaar, T., Sturmann, L., & McAlister, H. A. 2010, in Society of Photo-Optical Instrumentation Engineers (SPIE) Conference Series, Vol. 7734, Society of Photo-Optical Instrumentation Engineers (SPIE) Conference Series, 3
Su, K. Y. L., Rieke, G. H., Stansberry, J. A., et al. 2006, ApJ, 653, 675
Tatulli, E., Millour, F., Chelli, A., et al. 2007, A&A, 464, 29
Taylor, A. R., Dougherty, S. M., Waters, L. B. F. M., & Bjorkman, K. S. 1990, A&A, 231, 453
Touhami, Y., Gies, D. R., & Schaefer, G. H. 2011, ApJ, 729, 17
Tycner, C., Benson, J. A., Hutter, D. J., Schmitt, H. R., & Zavala, R. T. 2006, in Society of Photo-Optical Instrumentation Engineers (SPIE) Conference Series, Vol. 6268, Society of Photo-Optical Instrumentation Engineers (SPIE) Conference Series, 49
Tycner, C., Hajian, A. R., Mozurkewich, D., et al. 2003, AJ, 125, 3378
Tycner, C., Jones, C. E., Sigut, T. A. A., et al. 2008, ApJ, 689, 461
Štefl, S., Carciofi, A. C., Baade, D., et al. 2011, in IAU Symposium, Vol. 272, IAU Symposium, ed. C. Neiner, G. Wade, G. Meynet, & G. Peters, 430–432
Štefl, S., LeBouquin, J.-B., Rivinius, T., et al. 2012, in Astronomical Society of the Pacific Conference Series, Vol. 464, Circumstellar Dynamics at High Resolution, ed. A. C. Carciofi & T. Rivinius, 197
van Leeuwen, F. 2007, A&A, 474, 653
Vieira, R. G., Carciofi, A. C., & Bjorkman, J. E. 2015, MNRAS
von Zeipel, H. 1924, MNRAS, 84, 665
Waters, L. B. F., Marlborough, J. M., van der Veen, W. E. C., Taylor, A. R., & Dougherty, S. M. 1991, A&A, 244, 120
Wheelwright, H. E., Bjorkman, J. E., Oudmaijer, R. D., et al. 2012, MNRAS, 423, L11

Table 3. OPD/LNA broadband polarimetry.

Date	Johnson filter	Polarization level (%)	Position Angle (°)
2011-10-20	B	0.039 ± 0.003	73.7 ± 2.0
2011-10-20	V	0.022 ± 0.015	51.5 ± 20.1
2011-10-20	R	0.050 ± 0.004	46.1 ± 2.3
2011-10-20	I	0.071 ± 0.019	57.0 ± 7.8
2012-04-04	V	0.027 ± 0.018	38.8 ± 18.6
2012-04-04	R	0.027 ± 0.015	37.8 ± 15.9
2012-04-04	I	0.049 ± 0.015	43.3 ± 8.8
2013-04-24	B	0.048 ± 0.076	37.6 ± 46.0
2013-04-24	V	0.038 ± 0.039	54.4 ± 29.1
2013-11-13	B	0.059 ± 0.064	43.3 ± 31.3
2013-11-13	V	0.060 ± 0.035	55.2 ± 16.7
2013-11-13	R	0.053 ± 0.024	41.8 ± 13.2
2013-11-13	I	0.078 ± 0.013	44.8 ± 4.8
2014-03-09	B	0.096 ± 0.143	67.0 ± 42.9
2014-03-09	V	0.042 ± 0.023	60.4 ± 15.9
2014-03-09	R	0.066 ± 0.024	51.8 ± 10.4
2014-03-09	I	0.038 ± 0.021	45.2 ± 15.6

Table 5. Calibrated NPOI Hα squared visibilities of β CMi.

Julian Date (JD - 2 450 000)	Spatial Frequency u (10^6 cycles rad^{-1})	Spatial Frequency v (10^6 cycles rad^{-1})	V^2	Baseline
5519.998	27.398	−8.902	0.946 ± 0.022	AC-AE
5519.998	58.731	39.487	0.770 ± 0.042	AC-W7
5519.998	86.129	30.584	0.677 ± 0.039	AE-W7
5519.998	50.868	−9.168	0.862 ± 0.048	AC-E6
5519.998	109.572	30.301	0.537 ± 0.027	E6-W7
5519.998	58.704	39.469	0.662 ± 0.032	AC-W7
5531.940	27.106	−9.530	0.863 ± 0.041	AC-AE
5531.940	64.257	38.071	0.786 ± 0.029	AC-W7
5531.940	91.363	28.541	0.645 ± 0.057	AE-W7
5531.940	51.103	−10.341	0.854 ± 0.062	AC-E6
5531.940	115.330	27.712	0.517 ± 0.129	E6-W7
5531.940	64.228	38.054	0.761 ± 0.055	AC-W7
5531.973	27.345	−8.704	0.893 ± 0.048	AC-AE
5531.973	56.669	39.905	0.804 ± 0.079	AC-W7
5531.973	84.014	31.201	0.937 ± 0.138	AE-W7
5531.973	50.524	−8.800	0.896 ± 0.089	AC-E6
5531.973	107.167	31.086	0.544 ± 0.229	E6-W7
5531.973	56.643	39.886	0.732 ± 0.098	AC-W7
5532.938	27.139	−9.497	0.971 ± 0.044	AC-AE
5532.938	64.007	38.148	0.814 ± 0.048	AC-W7
5532.938	91.146	28.651	0.733 ± 0.068	AE-W7
5532.938	51.123	−10.280	0.890 ± 0.075	AC-E6
5532.938	115.100	27.851	0.751 ± 0.078	E6-W7
5532.938	63.978	38.131	0.864 ± 0.038	AC-W7
5532.956	27.391	−9.054	1.015 ± 0.053	AC-AE
5532.956	60.210	39.156	0.793 ± 0.048	AC-W7
5532.956	87.602	30.101	0.764 ± 0.131	AE-W7
5532.956	51.044	−9.451	0.840 ± 0.028	AC-E6
5532.956	111.227	29.687	0.658 ± 0.060	E6-W7
5532.956	60.183	39.138	0.867 ± 0.033	AC-W7
5532.981	27.170	−8.445	0.974 ± 0.051	AC-AE
5532.981	53.749	40.429	0.857 ± 0.052	AC-W7
5532.981	80.919	31.984	0.761 ± 0.065	AE-W7
5532.981	49.879	−8.323	0.849 ± 0.061	AC-E6
5532.981	103.603	32.087	0.847 ± 0.088	E6-W7
5532.981	53.725	40.411	0.867 ± 0.039	AC-W7
5537.948	27.399	−8.921	0.966 ± 0.051	AC-AE
5537.948	50.894	−9.203	0.646 ± 0.277	AC-E6
5537.948	109.787	30.225	0.711 ± 0.149	E6-W7
5537.948	58.893	39.427	0.774 ± 0.146	AC-W7
5538.920	27.085	−9.550	0.934 ± 0.041	AC-AE
5538.920	64.411	38.022	0.736 ± 0.034	AC-W7
5538.920	91.496	28.472	0.700 ± 0.051	AE-W7
5538.920	51.088	−10.380	0.730 ± 0.060	AC-E6
5538.920	115.470	27.625	0.670 ± 0.040	E6-W7
5538.920	64.382	38.005	0.752 ± 0.027	AC-W7
5538.946	27.398	−8.906	0.880 ± 0.035	AC-AE
5538.946	58.768	39.478	0.689 ± 0.049	AC-W7
5538.946	86.166	30.572	0.801 ± 0.112	AE-W7
5538.946	50.873	−9.175	0.800 ± 0.074	AC-E6
5538.946	109.614	30.285	0.652 ± 0.042	E6-W7
5538.946	58.741	39.460	0.838 ± 0.058	AC-W7
5540.969	49.102	−7.896	0.877 ± 0.023	AC-E6
5541.916	27.180	−9.453	0.881 ± 0.091	AC-AE
5541.924	27.330	−9.235	0.858 ± 0.096	AC-AE
5541.924	89.181	29.518	0.476 ± 0.236	AE-W7
5541.924	51.155	−9.788	0.846 ± 0.139	AC-E6
5541.924	112.977	28.947	0.682 ± 0.216	E6-W7
5541.956	27.167	−8.442	0.841 ± 0.111	AC-AE

Table 5. Continued.

Julian Date (JD - 2 450 000)	Spatial Frequency u (10^6 cycles rad^{-1})	Spatial Frequency v (10^6 cycles rad^{-1})	V^2	Baseline
5541.956	49.870	-8.318	1.076 ± 0.134	AC-E6
5541.956	103.558	32.099	0.852 ± 0.226	E6-W7
5543.939	27.361	-8.744	0.882 ± 0.029	AC-AE
5543.939	57.097	39.821	0.890 ± 0.077	AC-W7
5543.939	84.458	31.077	0.765 ± 0.057	AE-W7
5543.939	50.604	-8.874	0.795 ± 0.104	AC-E6
5543.939	107.674	30.929	0.676 ± 0.030	E6-W7
5543.939	57.071	39.803	0.787 ± 0.052	AC-W7
5567.865	27.400	-8.957	0.920 ± 0.042	AC-AE
5567.865	50.941	-9.270	0.814 ± 0.050	AC-E6
5567.865	110.190	30.079	0.601 ± 0.143	E6-W7
5574.804	26.475	-9.969	0.941 ± 0.037	AC-AE
5574.804	67.209	36.991	0.774 ± 0.091	AC-W7
5574.804	93.684	27.022	0.771 ± 0.064	AE-W7
5574.804	50.473	-11.175	0.793 ± 0.048	AC-E6
5574.804	117.651	25.799	0.475 ± 0.059	E6-W7
5574.804	67.178	36.974	0.828 ± 0.053	AC-W7
5575.810	26.808	-9.769	0.952 ± 0.019	AC-AE
5575.810	65.960	37.492	0.816 ± 0.030	AC-W7
5575.810	92.768	27.724	0.700 ± 0.042	AE-W7
5575.810	50.844	-10.794	0.940 ± 0.067	AC-E6
5575.810	116.774	26.682	0.575 ± 0.091	E6-W7
5575.810	65.930	37.475	0.778 ± 0.071	AC-W7
5575.874	26.866	-8.180	0.917 ± 0.038	AC-AE
5575.874	50.493	40.939	0.768 ± 0.092	AC-W7
5575.874	77.358	32.758	0.727 ± 0.086	AE-W7
5575.874	50.470	40.920	0.897 ± 0.086	AC-W7
5576.799	26.464	-9.975	0.908 ± 0.017	AC-AE
5576.799	67.243	36.976	0.815 ± 0.035	AC-W7
5576.799	93.707	27.000	0.746 ± 0.036	AE-W7
5576.799	50.459	-11.187	0.847 ± 0.046	AC-E6
5576.799	117.672	25.772	0.641 ± 0.045	E6-W7
5576.799	67.213	36.959	0.724 ± 0.046	AC-W7
5577.838	27.400	-8.941	0.958 ± 0.025	AC-AE
5577.838	50.920	-9.240	0.914 ± 0.057	AC-E6
5577.846	27.357	-8.733	1.036 ± 0.036	AC-AE
5577.846	56.980	39.843	0.815 ± 0.075	AC-W7
5577.846	84.337	31.110	0.852 ± 0.073	AE-W7
5577.846	50.582	-8.854	0.940 ± 0.055	AC-E6
5577.846	107.536	30.971	0.671 ± 0.056	E6-W7
5577.846	56.954	39.825	0.859 ± 0.064	AC-W7
5578.832	27.397	-9.012	0.869 ± 0.074	AC-AE
5578.840	27.383	-8.815	0.848 ± 0.157	AC-AE
5578.853	27.223	-8.508	0.905 ± 0.050	AC-AE
5597.765	27.240	-9.386	0.900 ± 0.032	AC-AE
5597.765	-63.128	-38.415	0.779 ± 0.090	AC-W7
5597.765	-90.368	-29.028	0.733 ± 0.046	AE-W7
5597.765	51.063	-10.049	0.899 ± 0.052	AC-E6
5597.765	-114.028	-28.266	0.631 ± 0.039	E6-W7
5597.765	-62.965	-38.315	0.812 ± 0.049	AC-W7
5597.787	27.397	-8.863	0.945 ± 0.052	AC-AE
5597.787	-58.329	-39.578	0.753 ± 0.108	AC-W7
5597.787	-85.726	-30.715	0.766 ± 0.105	AE-W7
5597.787	50.708	-9.075	0.911 ± 0.072	AC-E6
5597.787	-108.886	-30.401	0.683 ± 0.080	E6-W7
5597.787	-58.179	-39.476	0.873 ± 0.090	AC-W7
5597.798	27.278	-8.579	0.941 ± 0.032	AC-AE
5597.798	-55.280	-40.169	0.792 ± 0.037	AC-W7
5597.798	-82.558	-31.591	0.841 ± 0.036	AE-W7
5597.798	50.136	-8.550	0.887 ± 0.046	AC-E6

Table 5. Continued.

Julian Date (JD - 2 450 000)	Spatial Frequency u (10^6 cycles rad^{-1})	Spatial Frequency v (10^6 cycles rad^{-1})	V^2	Baseline
5597.798	-105.273	-31.516	0.655 ± 0.032	E6-W7
5597.798	-55.137	-40.065	0.826 ± 0.043	AC-W7
5597.802	27.213	-8.491	0.980 ± 0.066	AC-AE
5597.802	49.908	-8.390	0.889 ± 0.086	AC-E6
5598.744	-66.474	-37.306	0.751 ± 0.204	AC-W7
5598.744	-93.166	-27.458	0.569 ± 0.156	AE-W7
5598.744	50.617	-10.919	0.803 ± 0.060	AC-E6
5598.744	-116.919	-26.290	0.862 ± 0.073	E6-W7
5598.744	-66.302	-37.209	0.869 ± 0.143	AC-W7
5598.792	27.328	-8.661	0.891 ± 0.035	AC-AE
5598.792	50.331	-8.702	0.716 ± 0.112	AC-E6
5598.795	27.279	-8.580	0.723 ± 0.139	AC-AE
5598.795	-55.294	-40.167	0.986 ± 0.142	AC-W7
5598.795	-82.573	-31.587	0.812 ± 0.138	AE-W7
5598.795	50.140	-8.552	0.953 ± 0.055	AC-E6
5598.795	-105.291	-31.511	0.888 ± 0.151	E6-W7
5598.795	-55.151	-40.063	1.040 ± 0.103	AC-W7
5599.740	26.645	-9.877	0.939 ± 0.028	AC-AE
5599.740	-66.653	-37.234	0.826 ± 0.042	AC-W7
5599.740	-93.298	-27.357	0.690 ± 0.043	AE-W7
5599.740	50.565	-10.974	0.819 ± 0.034	AC-E6
5599.740	-117.046	-26.164	0.588 ± 0.031	E6-W7
5599.740	-66.481	-37.138	0.744 ± 0.041	AC-W7
5599.758	27.209	-9.425	0.978 ± 0.022	AC-AE
5599.758	-63.441	-38.325	0.788 ± 0.034	AC-W7
5599.758	-90.650	-28.900	0.707 ± 0.025	AE-W7
5599.758	51.054	-10.122	0.838 ± 0.029	AC-E6
5599.758	-114.330	-28.104	0.615 ± 0.020	E6-W7
5599.758	-63.277	-38.226	0.746 ± 0.030	AC-W7
5599.761	27.261	-9.358	0.898 ± 0.028	AC-AE
5599.761	-62.899	-38.479	0.799 ± 0.033	AC-W7
5599.761	-90.159	-29.121	0.766 ± 0.032	AE-W7
5599.761	51.067	-9.997	0.883 ± 0.021	AC-E6
5599.761	-113.803	-28.383	0.608 ± 0.017	E6-W7
5599.761	-62.736	-38.380	0.727 ± 0.025	AC-W7
5599.782	27.394	-8.849	0.912 ± 0.034	AC-AE
5599.782	-58.183	-39.609	0.848 ± 0.056	AC-W7
5599.782	-85.577	-30.760	0.749 ± 0.056	AE-W7
5599.782	50.685	-9.048	0.861 ± 0.030	AC-E6
5599.782	-108.717	-30.458	0.600 ± 0.032	E6-W7
5599.782	-58.032	-39.506	0.711 ± 0.033	AC-W7
5599.786	27.362	-8.737	0.927 ± 0.045	AC-AE
5599.786	-57.012	-39.844	0.776 ± 0.061	AC-W7
5599.786	-84.373	-31.108	0.793 ± 0.074	AE-W7
5599.786	50.486	-8.841	0.865 ± 0.032	AC-E6
5599.786	-107.351	-30.901	0.592 ± 0.034	E6-W7
5599.786	-56.864	-39.741	0.709 ± 0.066	AC-W7
5599.803	27.045	-8.321	0.878 ± 0.036	AC-AE
5599.803	-52.245	-40.680	0.860 ± 0.061	AC-W7
5599.803	-79.290	-32.359	0.747 ± 0.057	AE-W7
5599.803	49.386	-8.077	0.859 ± 0.033	AC-E6
5599.803	-101.496	-32.497	0.618 ± 0.027	E6-W7
5599.803	-52.110	-40.575	0.762 ± 0.039	AC-W7
5601.735	26.658	-9.869	0.871 ± 0.034	AC-AE
5601.735	50.579	-10.959	0.810 ± 0.028	AC-E6
5601.758	27.303	-9.295	0.906 ± 0.053	AC-AE
5601.758	51.066	-9.878	0.807 ± 0.041	AC-E6
5601.762	27.350	-9.203	0.919 ± 0.041	AC-AE
5601.762	51.041	-9.707	0.878 ± 0.033	AC-E6
5601.792	27.181	-8.455	0.886 ± 0.038	AC-AE

Table 5. Continued.

Julian Date (JD - 2 450 000)	Spatial Frequency u (10^6 cycles rad^{-1})	Spatial Frequency v (10^6 cycles rad^{-1})	V^2	Baseline
5601.792	49.804	−8.322	0.806 ± 0.036	AC-E6
5602.733	26.708	−9.838	0.913 ± 0.012	AC-AE
5602.733	−66.413	−37.329	0.827 ± 0.039	AC-W7
5602.733	−93.121	−27.491	0.739 ± 0.032	AE-W7
5602.733	50.634	−10.901	0.907 ± 0.028	AC-E6
5602.733	−116.875	−26.332	0.585 ± 0.025	E6-W7
5602.733	−66.241	−37.233	0.853 ± 0.040	AC-W7
5602.758	27.332	−9.242	0.923 ± 0.026	AC-AE
5602.758	−61.910	−38.745	0.799 ± 0.040	AC-W7
5602.758	−89.241	−29.503	0.737 ± 0.032	AE-W7
5602.758	51.055	−9.779	0.815 ± 0.046	AC-E6
5602.758	−112.805	−28.866	0.577 ± 0.030	E6-W7
5602.758	−61.750	−38.645	0.797 ± 0.040	AC-W7
5602.766	27.399	−9.035	0.916 ± 0.040	AC-AE
5602.766	−60.026	−39.206	0.855 ± 0.047	AC-W7
5602.766	−87.425	−30.170	0.739 ± 0.033	AE-W7
5602.766	50.924	−9.394	0.872 ± 0.026	AC-E6
5602.766	−110.795	−29.710	0.671 ± 0.015	E6-W7
5602.766	−59.871	−39.104	0.799 ± 0.032	AC-W7
5602.777	27.368	−8.752	0.898 ± 0.035	AC-AE
5602.777	−57.181	−39.811	0.876 ± 0.047	AC-W7
5602.777	−84.548	−31.059	0.784 ± 0.031	AE-W7
5602.777	50.517	−8.870	0.895 ± 0.037	AC-E6
5602.777	−107.550	−30.838	0.625 ± 0.020	E6-W7
5602.777	−57.033	−39.708	0.821 ± 0.037	AC-W7
5602.781	27.334	−8.673	0.910 ± 0.027	AC-AE
5602.781	−56.328	−39.976	0.868 ± 0.030	AC-W7
5602.781	−83.662	−31.303	0.741 ± 0.016	AE-W7
5602.781	50.356	−8.724	0.903 ± 0.023	AC-E6
5602.781	−106.539	−31.149	0.660 ± 0.024	E6-W7
5602.781	−56.183	−39.873	0.797 ± 0.032	AC-W7
5602.791	27.141	−8.412	0.942 ± 0.025	AC-AE
5602.791	49.677	−8.244	0.839 ± 0.053	AC-E6
5603.737	26.936	−9.681	0.929 ± 0.016	AC-AE
5603.737	−65.362	−37.716	0.887 ± 0.040	AC-W7
5603.737	−92.297	−28.035	0.637 ± 0.033	AE-W7
5603.737	50.863	−10.603	0.847 ± 0.041	AC-E6
5603.737	−116.056	−27.015	0.604 ± 0.039	E6-W7
5603.737	−65.193	−37.619	0.827 ± 0.026	AC-W7
5603.744	27.123	−9.518	0.879 ± 0.033	AC-AE
5603.744	−64.172	−38.105	1.048 ± 0.063	AC-W7
5603.744	−91.295	−28.587	0.668 ± 0.036	AE-W7
5603.744	51.010	−10.297	0.843 ± 0.044	AC-E6
5603.744	−115.016	−27.710	0.609 ± 0.041	E6-W7
5603.744	−64.006	−38.007	0.870 ± 0.027	AC-W7
5603.768	27.403	−8.921	0.945 ± 0.031	AC-AE
5603.768	−58.912	−39.454	1.034 ± 0.095	AC-W7
5603.768	−86.315	−30.533	0.720 ± 0.045	AE-W7
5603.768	50.791	−9.182	0.775 ± 0.070	AC-E6
5603.768	−109.551	−30.170	0.545 ± 0.094	E6-W7
5603.768	−58.760	−39.352	0.806 ± 0.042	AC-W7
5603.771	27.394	−8.850	0.913 ± 0.025	AC-AE
5603.771	−58.192	−39.606	0.878 ± 0.060	AC-W7
5603.771	−85.587	−30.757	0.683 ± 0.045	AE-W7
5603.771	50.687	−9.050	0.913 ± 0.068	AC-E6
5603.771	−108.728	−30.454	0.664 ± 0.098	E6-W7
5603.771	−58.042	−39.504	0.845 ± 0.059	AC-W7
5603.782	27.275	−8.573	0.962 ± 0.032	AC-AE
5603.782	−55.221	−40.180	0.957 ± 0.050	AC-W7
5603.782	−82.495	−31.607	0.654 ± 0.031	AE-W7

Table 5. Continued.

Julian Date (JD - 2 450 000)	Spatial Frequency u (10^6 cycles rad^{-1})	Spatial Frequency v (10^6 cycles rad^{-1})	V^2	Baseline
5603.782	50.123	−8.540	0.842 ± 0.074	AC-E6
5603.782	−105.201	−31.536	0.666 ± 0.067	E6-W7
5603.782	−55.078	−40.076	0.845 ± 0.045	AC-W7
5603.785	27.213	−8.491	0.897 ± 0.041	AC-AE
5603.785	−54.281	−40.345	0.925 ± 0.083	AC-W7
5603.785	−81.494	−31.854	0.683 ± 0.045	AE-W7
5603.785	49.907	−8.389	0.884 ± 0.078	AC-E6
5603.785	−104.048	−31.851	0.735 ± 0.078	E6-W7
5603.785	−54.140	−40.241	0.848 ± 0.043	AC-W7
5604.732	26.869	−9.731	0.956 ± 0.041	AC-AE
5604.732	−65.706	−37.594	0.803 ± 0.043	AC-W7
5604.732	−92.575	−27.864	0.728 ± 0.065	AE-W7
5604.732	50.800	−10.698	0.817 ± 0.039	AC-E6
5604.732	−116.336	−26.799	0.623 ± 0.039	E6-W7
5604.732	−65.536	−37.497	0.838 ± 0.042	AC-W7
5604.739	27.079	−9.561	0.933 ± 0.040	AC-AE
5604.739	−64.493	−38.005	0.783 ± 0.041	AC-W7
5604.739	−91.572	−28.444	0.680 ± 0.061	AE-W7
5604.739	50.980	−10.377	0.846 ± 0.041	AC-E6
5604.739	−115.306	−27.529	0.637 ± 0.025	E6-W7
5604.739	−64.326	−37.906	0.792 ± 0.030	AC-W7
5604.748	27.269	−9.347	0.995 ± 0.035	AC-AE
5604.748	−62.804	−38.505	0.833 ± 0.054	AC-W7
5604.748	−90.072	−29.158	0.684 ± 0.066	AE-W7
5604.748	51.068	−9.976	0.863 ± 0.047	AC-E6
5604.748	−113.709	−28.430	0.592 ± 0.035	E6-W7
5604.748	−62.641	−38.406	0.734 ± 0.062	AC-W7
5604.751	27.322	−9.260	0.906 ± 0.040	AC-AE
5604.751	−62.068	−38.704	0.864 ± 0.056	AC-W7
5604.751	−89.390	−29.444	0.724 ± 0.069	AE-W7
5604.751	51.060	−9.813	0.824 ± 0.078	AC-E6
5604.751	−112.967	−28.791	0.699 ± 0.058	E6-W7
5604.751	−61.907	−38.604	0.772 ± 0.070	AC-W7
5604.776	27.326	−8.658	0.859 ± 0.051	AC-AE
5604.776	−56.159	−40.008	0.788 ± 0.082	AC-W7
5604.776	−83.484	−31.350	0.807 ± 0.060	AE-W7
5604.776	50.322	−8.695	0.846 ± 0.066	AC-E6
5604.776	−106.335	−31.209	0.638 ± 0.041	E6-W7
5604.776	−56.014	−39.904	0.862 ± 0.062	AC-W7
5604.779	27.281	−8.583	0.921 ± 0.039	AC-AE
5604.779	−55.327	−40.161	0.857 ± 0.039	AC-W7
5604.779	−82.608	−31.578	0.751 ± 0.041	AE-W7
5604.779	50.147	−8.557	0.832 ± 0.044	AC-E6
5604.779	−105.331	−31.499	0.641 ± 0.027	E6-W7
5604.779	−55.184	−40.057	0.775 ± 0.038	AC-W7
5604.789	27.065	−8.338	0.983 ± 0.051	AC-AE
5604.789	−52.462	−40.645	0.814 ± 0.070	AC-W7
5604.789	−79.527	−32.307	0.826 ± 0.085	AE-W7
5604.789	49.445	−8.110	0.950 ± 0.042	AC-E6
5604.789	−101.771	−32.431	0.738 ± 0.040	E6-W7
5604.789	−52.326	−40.540	0.908 ± 0.036	AC-W7
5604.792	26.966	−8.254	0.924 ± 0.041	AC-AE
5604.792	−51.417	−40.808	0.921 ± 0.089	AC-W7
5604.792	−78.383	−32.554	0.859 ± 0.129	AE-W7
5604.792	49.156	−7.956	0.785 ± 0.036	AC-E6
5604.792	−100.440	−32.747	0.712 ± 0.042	E6-W7
5604.792	−51.284	−40.702	0.841 ± 0.059	AC-W7
5605.728	26.803	−9.772	0.894 ± 0.030	AC-AE
5605.728	−65.984	−37.484	0.978 ± 0.112	AC-W7
5605.728	−92.786	−27.711	0.905 ± 0.132	AE-W7

Table 5. Continued.

Julian Date (JD - 2 450 000)	Spatial Frequency u (10^6 cycles rad^{-1})	Spatial Frequency v (10^6 cycles rad^{-1})	V^2	Baseline
5605.728	50.839	−10.800	0.852 ± 0.054	AC-E6
5605.728	−116.792	−26.666	0.468 ± 0.114	E6-W7
5605.728	−65.953	−37.466	0.747 ± 0.124	AC-W7
5605.735	27.020	−9.608	0.897 ± 0.027	AC-AE
5605.735	−64.843	−37.882	0.889 ± 0.078	AC-W7
5605.735	−91.863	−28.274	0.851 ± 0.092	AE-W7
5605.735	51.039	−10.490	0.855 ± 0.036	AC-E6
5605.735	−115.853	−27.375	0.621 ± 0.105	E6-W7
5605.735	−64.813	−37.865	0.763 ± 0.058	AC-W7
5605.744	27.237	−9.383	0.911 ± 0.038	AC-AE
5605.744	−63.104	−38.413	0.736 ± 0.103	AC-W7
5605.744	−90.342	−29.029	0.962 ± 0.141	AE-W7
5605.744	51.165	−10.066	0.859 ± 0.038	AC-E6
5605.744	−114.240	−28.329	0.686 ± 0.098	E6-W7
5605.744	−63.076	−38.395	0.717 ± 0.075	AC-W7
5605.746	27.286	−9.314	0.888 ± 0.029	AC-AE
5605.746	−62.529	−38.572	0.779 ± 0.108	AC-W7
5605.746	−89.815	−29.258	0.750 ± 0.073	AE-W7
5605.746	51.169	−9.936	0.833 ± 0.054	AC-E6
5605.746	−113.669	−28.619	0.570 ± 0.060	E6-W7
5605.746	−62.500	−38.555	0.714 ± 0.062	AC-W7
5605.756	27.387	−9.078	0.908 ± 0.036	AC-AE
5605.756	−60.428	−39.104	0.836 ± 0.131	AC-W7
5605.756	−87.814	−30.026	0.896 ± 0.100	AE-W7
5605.756	51.064	−9.494	0.828 ± 0.045	AC-E6
5605.756	−111.465	−29.592	0.632 ± 0.050	E6-W7
5605.756	−60.400	−39.086	0.814 ± 0.056	AC-W7
5605.759	27.397	−9.013	0.867 ± 0.030	AC-AE
5605.759	−59.819	−39.245	0.494 ± 0.150	AC-W7
5605.759	−87.216	−30.232	0.921 ± 0.178	AE-W7
5605.759	51.004	−9.374	0.893 ± 0.030	AC-E6
5605.759	−110.795	−29.853	0.679 ± 0.146	E6-W7
5605.759	−59.791	−39.227	0.673 ± 0.085	AC-W7
5605.773	27.316	−8.647	0.911 ± 0.026	AC-AE
5605.773	−56.047	−40.021	0.907 ± 0.082	AC-W7
5605.773	−83.363	−31.374	0.828 ± 0.089	AE-W7
5605.773	50.401	−8.695	0.903 ± 0.044	AC-E6
5605.773	−106.422	−31.308	0.711 ± 0.083	E6-W7
5605.773	−56.021	−40.003	0.722 ± 0.049	AC-W7
5605.776	27.280	−8.587	0.913 ± 0.026	AC-AE
5605.776	−55.379	−40.144	0.987 ± 0.065	AC-W7
5605.776	−82.660	−31.557	0.668 ± 0.089	AE-W7
5605.776	50.259	−8.584	0.883 ± 0.054	AC-E6
5605.776	−105.613	−31.541	0.560 ± 0.080	E6-W7
5605.776	−55.354	−40.125	0.781 ± 0.044	AC-W7
5605.789	26.973	−8.262	0.881 ± 0.023	AC-AE
5605.789	−51.524	−40.784	0.915 ± 0.230	AC-W7
5605.789	−78.497	−32.522	0.457 ± 0.160	AE-W7
5605.789	49.286	−7.988	0.913 ± 0.040	AC-E6
5605.789	−100.787	−32.777	0.561 ± 0.199	E6-W7
5605.789	−51.501	−40.765	0.689 ± 0.168	AC-W7
5607.742	27.299	−9.300	0.898 ± 0.042	AC-AE
5607.752	27.398	−9.040	0.871 ± 0.058	AC-AE
5607.752	50.928	−9.402	0.843 ± 0.086	AC-E6
5607.766	27.341	−8.688	0.886 ± 0.043	AC-AE
5607.766	50.388	−8.751	0.895 ± 0.070	AC-E6
5607.783	27.002	−8.284	0.887 ± 0.034	AC-AE
5607.783	−51.790	−40.751	0.690 ± 0.175	AC-W7
5607.783	−78.792	−32.467	0.845 ± 0.183	AE-W7
5607.783	−51.656	−40.645	0.717 ± 0.101	AC-W7

Table 5. Continued.

Julian Date (JD - 2 450 000)	Spatial Frequency u (10^6 cycles rad^{-1})	Spatial Frequency v (10^6 cycles rad^{-1})	V^2	Baseline
5608.760	−27.375	8.787	0.920 ± 0.052	AC-AE
5608.760	57.548	39.730	1.100 ± 0.125	AC-W7
5608.760	−84.924	−30.943	0.823 ± 0.111	AE-W7
5608.760	−50.683	8.954	0.792 ± 0.049	AC-E6
5608.760	−108.205	−30.758	0.551 ± 0.056	E6-W7
5608.760	57.522	39.712	0.666 ± 0.088	AC-W7
5615.632	−21.961	11.324	0.960 ± 0.030	AC-AE
5615.632	−43.735	13.798	0.840 ± 0.056	AC-E6
5615.632	74.989	−2.222	0.807 ± 0.031	AW-E6
5615.632	31.254	11.576	0.933 ± 0.042	AC-AW
5615.638	−22.610	11.194	0.932 ± 0.027	AC-AE
5615.638	−44.780	13.540	0.825 ± 0.031	AC-E6
5615.638	76.175	−1.780	0.809 ± 0.039	AW-E6
5615.638	31.395	11.759	0.882 ± 0.027	AC-AW
5621.628	−23.207	11.063	0.867 ± 0.206	AC-AE
5621.687	−26.919	9.717	0.910 ± 0.115	AC-AE
5621.716	−27.424	9.001	0.912 ± 0.037	AC-AE
5621.716	−51.013	9.342	0.855 ± 0.041	AC-E6
5621.716	78.646	5.004	0.742 ± 0.070	AW-E6
5621.716	27.633	14.346	0.830 ± 0.071	AC-AW
5621.719	−27.424	8.932	0.964 ± 0.045	AC-AE
5621.719	−50.928	9.213	0.846 ± 0.034	AC-E6
5621.719	78.291	5.202	0.792 ± 0.086	AW-E6
5621.719	27.362	14.415	0.850 ± 0.094	AC-AW
5621.729	−27.345	8.661	0.925 ± 0.037	AC-AE
5621.729	−50.445	8.712	0.882 ± 0.040	AC-E6
5621.729	26.222	14.680	0.630 ± 0.161	AC-AW
5621.736	−27.237	8.502	0.923 ± 0.030	AC-AE
5621.736	−50.048	8.418	0.865 ± 0.039	AC-E6
5621.736	25.490	14.831	0.729 ± 0.104	AC-AW
5622.683	−26.873	9.750	0.896 ± 0.022	AC-AE
5622.683	−50.916	10.747	0.804 ± 0.076	AC-E6
5622.683	80.928	2.804	0.698 ± 0.038	AW-E6
5622.683	30.012	13.551	0.886 ± 0.035	AC-AW
5622.685	−26.954	9.690	0.922 ± 0.020	AC-AE
5622.685	−50.993	10.634	0.886 ± 0.046	AC-E6
5622.685	80.853	2.983	0.738 ± 0.041	AW-E6
5622.685	29.860	13.617	0.896 ± 0.029	AC-AW
5622.695	−27.212	9.453	0.911 ± 0.030	AC-AE
5622.695	−51.179	10.187	0.883 ± 0.045	AC-E6
5622.695	80.369	3.689	0.728 ± 0.028	AW-E6
5622.695	29.190	13.876	0.927 ± 0.031	AC-AW
5622.698	−27.283	9.364	0.894 ± 0.027	AC-AE
5622.698	−51.200	10.020	0.885 ± 0.053	AC-E6
5622.698	80.112	3.951	0.788 ± 0.038	AW-E6
5622.698	28.913	13.971	0.896 ± 0.041	AC-AW
5622.709	−27.405	9.112	0.933 ± 0.021	AC-AE
5622.709	−51.116	9.549	0.869 ± 0.031	AC-E6
5622.709	79.167	4.683	0.772 ± 0.027	AW-E6
5622.709	28.051	14.233	0.940 ± 0.029	AC-AW
5622.711	−27.418	9.054	0.925 ± 0.019	AC-AE
5622.711	−51.067	9.441	0.889 ± 0.047	AC-E6
5622.711	78.902	4.852	0.708 ± 0.035	AW-E6
5622.711	27.835	14.292	0.883 ± 0.032	AC-AW
5622.713	−27.424	8.995	0.912 ± 0.022	AC-AE
5622.713	−51.006	9.330	0.834 ± 0.038	AC-E6
5622.713	78.614	5.022	0.715 ± 0.026	AW-E6
5622.713	27.609	14.352	0.868 ± 0.025	AC-AW
5622.724	−27.381	8.740	0.918 ± 0.022	AC-AE
5622.724	−50.611	8.858	0.839 ± 0.028	AC-E6

Table 5. Continued.

Julian Date (JD - 2 450 000)	Spatial Frequency u (10^6 cycles rad^{-1})	Spatial Frequency v (10^6 cycles rad^{-1})	V^2	Baseline
5622.724	77.179	5.746	0.749 ± 0.035	AW-E6
5622.724	26.568	14.604	0.904 ± 0.032	AC-AW
5622.726	-27.355	8.681	0.922 ± 0.012	AC-AE
5622.726	-50.489	8.749	0.871 ± 0.030	AC-E6
5622.726	76.800	5.912	0.738 ± 0.034	AW-E6
5622.726	26.311	14.661	0.889 ± 0.037	AC-AW
5622.736	-27.185	8.442	0.930 ± 0.018	AC-AE
5622.736	-49.878	8.309	0.859 ± 0.024	AC-E6
5622.736	75.083	6.577	0.716 ± 0.024	AW-E6
5622.736	25.206	14.886	0.900 ± 0.027	AC-AW
5624.650	-25.523	10.405	0.901 ± 0.031	AC-AE
5624.650	-49.218	12.000	0.887 ± 0.032	AC-E6
5624.679	-26.932	9.707	0.904 ± 0.013	AC-AE
5624.679	-50.972	10.666	0.838 ± 0.027	AC-E6
5624.685	-27.113	9.555	0.931 ± 0.026	AC-AE
5624.685	-51.122	10.380	0.782 ± 0.032	AC-E6
5624.706	-27.421	9.032	0.908 ± 0.016	AC-AE
5624.706	-51.046	9.399	0.833 ± 0.029	AC-E6
5624.713	-27.418	8.876	0.909 ± 0.012	AC-AE
5624.713	-50.848	9.109	0.872 ± 0.024	AC-E6
5626.725	27.294	-8.476	0.965 ± 0.022	AC-AE
5629.645	26.146	-10.239	1.015 ± 0.041	AC-AE
5629.645	50.049	-11.631	0.831 ± 0.140	AC-E6
5629.645	81.063	1.435	0.797 ± 0.042	AW-E6
5629.645	31.014	13.066	0.873 ± 0.047	AC-AW
5629.654	26.591	-10.026	0.924 ± 0.048	AC-AE
5629.654	81.234	2.092	0.825 ± 0.117	AW-E6
5629.654	30.623	13.315	0.867 ± 0.034	AC-AW
5629.671	27.207	-9.607	0.973 ± 0.057	AC-AE
5629.671	80.839	3.354	0.821 ± 0.144	AW-E6
5629.671	29.602	13.784	0.849 ± 0.055	AC-AW
5629.675	27.307	-9.506	0.871 ± 0.039	AC-AE
5629.675	80.607	3.651	0.971 ± 0.082	AW-E6
5629.675	29.310	13.893	0.883 ± 0.048	AC-AW
5629.695	27.534	-9.016	0.933 ± 0.030	AC-AE
5629.695	51.114	-9.326	0.976 ± 0.043	AC-E6
5629.695	78.733	5.076	0.790 ± 0.033	AW-E6
5629.695	27.620	14.402	0.821 ± 0.033	AC-AW
5629.697	27.532	-8.951	0.935 ± 0.045	AC-AE
5629.697	51.031	-9.206	0.883 ± 0.138	AC-E6
5629.697	78.397	5.260	0.793 ± 0.066	AW-E6
5629.697	27.366	14.466	0.870 ± 0.051	AC-AW
5629.713	27.360	-8.554	0.965 ± 0.070	AC-AE
5629.713	50.220	-8.473	0.984 ± 0.182	AC-E6
5629.713	75.859	6.377	0.822 ± 0.067	AW-E6
5629.713	25.639	14.850	0.912 ± 0.059	AC-AW
5629.716	27.310	-8.495	0.958 ± 0.035	AC-AE
5629.716	50.055	-8.364	0.906 ± 0.066	AC-E6
5629.716	75.413	6.541	0.788 ± 0.038	AW-E6
5629.716	25.358	14.905	0.866 ± 0.031	AC-AW
5630.658	-26.758	9.827	0.918 ± 0.025	AC-AE
5630.658	-50.798	10.893	0.876 ± 0.037	AC-E6
5630.658	80.997	2.572	0.769 ± 0.028	AW-E6
5630.658	30.199	13.465	0.906 ± 0.025	AC-AW
5630.671	-51.161	10.260	0.830 ± 0.035	AC-E6
5630.671	80.468	3.574	0.731 ± 0.014	AW-E6
5630.671	29.307	13.834	0.923 ± 0.038	AC-AW
5630.693	-27.425	8.957	0.914 ± 0.016	AC-AE
5630.693	-50.960	9.259	0.834 ± 0.030	AC-E6
5630.693	78.421	5.131	0.769 ± 0.023	AW-E6

Table 5. Continued.

Julian Date (JD - 2 450 000)	Spatial Frequency *u* (10^6 cycles rad^{-1})	Spatial Frequency *v* (10^6 cycles rad^{-1})	V^2	Baseline
5630.693	27.461	14.390	0.963 ± 0.043	AC-AW
5630.695	−27.421	8.898	0.946 ± 0.024	AC-AE
5630.695	−50.880	9.150	0.848 ± 0.028	AC-E6
5630.695	78.106	5.300	0.702 ± 0.028	AW-E6
5630.695	27.226	14.449	0.925 ± 0.037	AC-AW
5630.709	−27.274	8.550	0.920 ± 0.018	AC-AE
5630.709	−50.176	8.507	0.848 ± 0.034	AC-E6
5630.709	75.892	6.279	0.715 ± 0.029	AW-E6
5630.709	25.715	14.786	0.903 ± 0.060	AC-AW
5633.659	−27.084	9.583	0.957 ± 0.028	AC-AE
5633.659	−51.100	10.432	0.831 ± 0.042	AC-E6
5633.659	80.671	3.303	0.742 ± 0.023	AW-E6
5633.659	29.571	13.735	0.905 ± 0.021	AC-AW
5633.666	−27.247	9.411	0.940 ± 0.027	AC-AE
5633.666	−51.192	10.108	0.799 ± 0.046	AC-E6
5633.666	80.252	3.813	0.756 ± 0.022	AW-E6
5633.666	29.060	13.921	0.924 ± 0.020	AC-AW
5633.675	−27.380	9.189	0.948 ± 0.024	AC-AE
5633.675	−51.164	9.693	0.845 ± 0.024	AC-E6
5633.675	79.490	4.461	0.746 ± 0.015	AW-E6
5633.675	28.326	14.153	0.948 ± 0.033	AC-AW
5633.678	−27.404	9.117	0.964 ± 0.023	AC-AE
5633.678	−51.120	9.557	0.822 ± 0.025	AC-E6
5633.678	79.186	4.671	0.756 ± 0.020	AW-E6
5633.678	28.066	14.228	0.956 ± 0.023	AC-AW
5633.686	−27.423	8.916	0.935 ± 0.022	AC-AE
5633.686	−50.907	9.184	0.856 ± 0.021	AC-E6
5633.686	78.208	5.246	0.753 ± 0.015	AW-E6
5633.686	27.301	14.431	0.937 ± 0.026	AC-AW
5633.689	−27.414	8.852	0.930 ± 0.027	AC-AE
5633.689	−50.811	9.065	0.884 ± 0.037	AC-E6
5633.689	77.852	5.429	0.756 ± 0.017	AW-E6
5633.689	27.041	14.494	0.960 ± 0.020	AC-AW
5633.697	−27.336	8.645	0.918 ± 0.021	AC-AE
5633.697	−50.409	8.683	0.828 ± 0.030	AC-E6
5633.697	76.560	6.013	0.755 ± 0.018	AW-E6
5633.697	26.151	14.695	0.937 ± 0.024	AC-AW
5633.700	−27.295	8.580	0.966 ± 0.021	AC-AE
5633.700	−50.253	8.562	0.844 ± 0.032	AC-E6
5633.700	76.108	6.195	0.786 ± 0.023	AW-E6
5633.700	25.855	14.757	0.955 ± 0.026	AC-AW
5633.709	−27.107	8.364	0.939 ± 0.025	AC-AE
5633.709	−49.637	8.167	0.813 ± 0.040	AC-E6
5633.709	74.460	6.792	0.812 ± 0.027	AW-E6
5633.709	24.823	14.958	0.920 ± 0.031	AC-AW
5635.650	−26.957	9.688	0.927 ± 0.031	AC-AE
5635.650	−50.996	10.630	0.846 ± 0.028	AC-E6
5635.650	80.850	2.990	0.704 ± 0.033	AW-E6
5635.650	29.854	13.620	0.911 ± 0.037	AC-AW
5635.658	−27.180	9.488	0.903 ± 0.040	AC-AE
5635.658	−51.163	10.253	0.860 ± 0.025	AC-E6
5635.658	80.460	3.585	0.757 ± 0.025	AW-E6
5635.658	29.297	13.838	0.950 ± 0.025	AC-AW
5635.669	−27.365	9.224	0.964 ± 0.035	AC-AE
5635.669	−51.179	9.758	0.866 ± 0.041	AC-E6
5635.669	79.628	4.359	0.729 ± 0.037	AW-E6
5635.669	28.448	14.117	0.930 ± 0.033	AC-AW
5635.671	−27.389	9.165	0.929 ± 0.040	AC-AE
5635.671	−51.151	9.648	0.907 ± 0.049	AC-E6
5635.671	79.392	4.531	0.766 ± 0.032	AW-E6

Table 5. Continued.

Julian Date (JD - 2 450 000)	Spatial Frequency u (10^6 cycles rad^{-1})	Spatial Frequency v (10^6 cycles rad^{-1})	V^2	Baseline
5635.671	28.240	14.179	0.955 ± 0.023	AC-AW
5635.681	−27.424	8.923	0.943 ± 0.030	AC-AE
5635.681	−50.917	9.197	0.844 ± 0.033	AC-E6
5635.681	78.245	5.227	0.709 ± 0.029	AW-E6
5635.681	27.328	14.424	0.898 ± 0.033	AC-AW
5635.683	−27.416	8.863	0.923 ± 0.033	AC-AE
5635.683	−50.829	9.086	0.850 ± 0.030	AC-E6
5635.683	77.915	5.397	0.755 ± 0.024	AW-E6
5635.683	27.086	14.483	0.922 ± 0.036	AC-AW
5635.692	−27.334	8.641	0.951 ± 0.037	AC-AE
5635.692	−50.401	8.676	0.882 ± 0.033	AC-E6
5635.692	76.535	6.023	0.734 ± 0.024	AW-E6
5635.692	26.135	14.699	0.909 ± 0.027	AC-AW
5635.695	−27.293	8.577	0.934 ± 0.021	AC-AE
5635.695	−50.246	8.557	0.903 ± 0.029	AC-E6
5635.695	76.087	6.204	0.769 ± 0.031	AW-E6
5635.695	25.841	14.760	0.925 ± 0.036	AC-AW
5635.703	−27.112	8.369	0.975 ± 0.018	AC-AE
5635.703	−49.652	8.175	0.930 ± 0.029	AC-E6
5635.703	74.499	6.778	0.739 ± 0.069	AW-E6
5635.703	24.847	14.954	0.809 ± 0.054	AC-AW
5635.706	−27.022	8.290	0.927 ± 0.052	AC-AE
5635.706	−49.387	8.030	0.885 ± 0.064	AC-E6
5635.706	73.832	6.996	0.775 ± 0.106	AW-E6
5635.706	24.445	15.026	0.803 ± 0.050	AC-AW
5636.642	−26.777	9.815	0.967 ± 0.019	AC-AE
5636.642	−50.817	10.870	0.891 ± 0.053	AC-E6
5636.642	80.988	2.608	0.780 ± 0.036	AW-E6
5636.642	30.170	13.478	0.909 ± 0.020	AC-AW
5636.649	−27.024	9.635	0.948 ± 0.034	AC-AE
5636.649	−51.053	10.529	0.838 ± 0.068	AC-E6
5636.649	80.766	3.149	0.761 ± 0.046	AW-E6
5636.649	29.713	13.678	0.879 ± 0.023	AC-AW
5636.659	−27.270	9.382	0.971 ± 0.025	AC-AE
5636.659	−51.198	10.053	0.864 ± 0.056	AC-E6
5636.659	80.166	3.899	0.743 ± 0.039	AW-E6
5636.659	28.969	13.952	0.904 ± 0.029	AC-AW
5636.662	−27.310	9.323	0.962 ± 0.027	AC-AE
5636.662	−51.200	9.944	0.811 ± 0.037	AC-E6
5636.662	79.982	4.070	0.734 ± 0.042	AW-E6
5636.662	28.781	14.013	0.948 ± 0.033	AC-AW
5636.674	−27.422	9.027	0.978 ± 0.017	AC-AE
5636.674	−51.040	9.389	0.820 ± 0.029	AC-E6
5636.674	78.771	4.931	0.741 ± 0.024	AW-E6
5636.674	27.731	14.320	0.968 ± 0.028	AC-AW
5636.676	−27.425	8.969	0.974 ± 0.023	AC-AE
5636.676	−50.976	9.282	0.831 ± 0.044	AC-E6
5636.676	78.485	5.095	0.727 ± 0.035	AW-E6
5636.676	27.509	14.378	0.903 ± 0.038	AC-AW
5636.686	−27.378	8.731	0.992 ± 0.024	AC-AE
5636.686	−50.594	8.842	0.859 ± 0.048	AC-E6
5636.686	77.124	5.771	0.753 ± 0.036	AW-E6
5636.686	26.530	14.612	0.920 ± 0.031	AC-AW
5636.688	−27.346	8.663	0.978 ± 0.020	AC-AE
5636.688	−50.450	8.716	0.898 ± 0.056	AC-E6
5636.688	76.681	5.962	0.812 ± 0.038	AW-E6
5636.688	26.232	14.678	0.943 ± 0.026	AC-AW
5636.698	−27.163	8.419	0.936 ± 0.042	AC-AE
5636.698	−49.807	8.266	0.860 ± 0.034	AC-E6
5636.698	74.899	6.642	0.739 ± 0.041	AW-E6

Table 5. Continued.

Julian Date (JD - 2 450 000)	Spatial Frequency u (10^6 cycles rad^{-1})	Spatial Frequency v (10^6 cycles rad^{-1})	V^2	Baseline
5636.698	25.092	14.908	0.958 ± 0.031	AC-AW
5639.645	−27.145	9.525	0.925 ± 0.027	AC-AE
5639.645	−51.143	10.322	0.762 ± 0.065	AC-E6
5639.645	80.547	3.476	0.777 ± 0.022	AW-E6
5639.645	29.404	13.798	0.944 ± 0.040	AC-AW
5639.666	−27.423	9.013	0.936 ± 0.020	AC-AE
5639.666	−51.026	9.364	0.778 ± 0.042	AC-E6
5639.666	78.706	4.969	0.789 ± 0.023	AW-E6
5639.666	27.680	14.333	0.984 ± 0.035	AC-AW
5639.674	−27.405	8.810	0.922 ± 0.023	AC-AE
5639.674	−50.741	8.988	0.815 ± 0.050	AC-E6
5639.674	77.609	5.547	0.768 ± 0.024	AW-E6
5639.674	26.868	14.535	0.991 ± 0.024	AC-AW
5639.677	−27.383	8.744	0.918 ± 0.025	AC-AE
5639.677	−50.619	8.865	0.775 ± 0.042	AC-E6
5639.677	77.204	5.735	0.760 ± 0.021	AW-E6
5639.677	26.586	14.600	0.942 ± 0.034	AC-AW
5639.688	−27.213	8.473	0.944 ± 0.024	AC-AE
5639.688	−49.968	8.367	0.822 ± 0.037	AC-E6
5639.688	75.324	6.491	0.784 ± 0.030	AW-E6
5639.688	25.356	14.857	0.934 ± 0.036	AC-AW
5648.635	−27.384	9.178	0.922 ± 0.023	AC-AE
5648.635	−51.158	9.673	0.881 ± 0.034	AC-E6
5648.635	79.447	4.492	0.791 ± 0.026	AW-E6
5648.635	28.288	14.165	0.932 ± 0.023	AC-AW
5648.641	−27.421	9.028	0.926 ± 0.016	AC-AE
5648.641	−51.042	9.393	0.873 ± 0.031	AC-E6
5648.641	78.780	4.925	0.762 ± 0.017	AW-E6
5648.641	27.738	14.318	0.919 ± 0.027	AC-AW
5648.651	−27.398	8.788	0.946 ± 0.025	AC-AE
5648.651	−50.702	8.947	0.870 ± 0.022	AC-E6
5648.651	77.476	5.610	0.778 ± 0.032	AW-E6
5648.651	26.774	14.557	0.934 ± 0.024	AC-AW
5648.654	−27.371	8.714	0.896 ± 0.017	AC-AE
5648.654	−50.559	8.810	0.891 ± 0.038	AC-E6
5648.654	77.017	5.818	0.773 ± 0.030	AW-E6
5648.654	26.457	14.629	0.985 ± 0.034	AC-AW
5648.662	−27.248	8.515	0.947 ± 0.018	AC-AE
5648.662	−50.085	8.443	0.858 ± 0.034	AC-E6
5648.662	75.639	6.375	0.778 ± 0.028	AW-E6
5648.662	25.554	14.818	0.955 ± 0.032	AC-AW
5648.664	−27.195	8.453	0.916 ± 0.017	AC-AE
5648.664	−49.909	8.329	0.893 ± 0.029	AC-E6
5648.664	75.165	6.548	0.740 ± 0.042	AW-E6
5648.664	25.257	14.877	0.932 ± 0.024	AC-AW
5649.626	−27.306	9.329	0.961 ± 0.021	AC-AE
5649.626	−51.201	9.955	0.842 ± 0.039	AC-E6
5649.626	80.001	4.053	0.754 ± 0.036	AW-E6
5649.626	28.800	14.007	0.940 ± 0.030	AC-AW
5649.632	−27.385	9.175	0.950 ± 0.013	AC-AE
5649.632	−51.157	9.667	0.824 ± 0.019	AC-E6
5649.632	79.434	4.501	0.801 ± 0.035	AW-E6
5649.632	28.277	14.168	0.914 ± 0.028	AC-AW
5649.641	−27.425	8.952	0.983 ± 0.020	AC-AE
5649.641	−50.954	9.250	0.905 ± 0.048	AC-E6
5649.641	78.396	5.145	0.804 ± 0.055	AW-E6
5649.641	27.442	14.395	0.886 ± 0.036	AC-AW
5649.644	−27.420	8.888	0.953 ± 0.015	AC-AE
5649.644	−50.866	9.131	0.861 ± 0.019	AC-E6
5649.644	78.051	5.328	0.752 ± 0.033	AW-E6

Table 5. Continued.

Julian Date (JD - 2 450 000)	Spatial Frequency u (10^6 cycles rad^{-1})	Spatial Frequency v (10^6 cycles rad^{-1})	V^2	Baseline
5649.644	27.185	14.459	0.949 ± 0.031	AC-AW
5649.653	−27.348	8.667	0.933 ± 0.023	AC-AE
5649.653	−50.459	8.724	0.868 ± 0.037	AC-E6
5649.653	76.710	5.950	0.777 ± 0.034	AW-E6
5649.653	26.251	14.674	0.971 ± 0.031	AC-AW
5649.655	−27.309	8.601	0.965 ± 0.016	AC-AE
5649.655	−50.305	8.601	0.826 ± 0.040	AC-E6
5649.655	76.258	6.136	0.781 ± 0.027	AW-E6
5649.655	25.952	14.737	0.923 ± 0.033	AC-AW
5649.664	−27.125	8.381	0.956 ± 0.026	AC-AE
5649.664	−49.691	8.198	0.832 ± 0.062	AC-E6
5649.664	74.599	6.745	0.847 ± 0.063	AW-E6
5649.664	24.907	14.943	0.902 ± 0.046	AC-AW
5650.624	−27.324	9.301	0.903 ± 0.026	AC-AE
5650.624	−51.198	9.902	0.850 ± 0.054	AC-E6
5650.624	79.906	4.135	0.701 ± 0.030	AW-E6
5650.624	28.707	14.037	0.930 ± 0.037	AC-AW
5650.635	−27.418	9.052	0.963 ± 0.048	AC-AE
5650.635	−51.065	9.437	0.840 ± 0.173	AC-E6
5650.635	78.893	4.857	0.874 ± 0.200	AW-E6
5650.635	27.828	14.294	0.877 ± 0.054	AC-AW
5650.645	−27.397	8.784	0.946 ± 0.023	AC-AE
5650.645	−50.694	8.939	0.912 ± 0.048	AC-E6
5650.645	77.450	5.622	0.714 ± 0.032	AW-E6
5650.645	26.756	14.561	0.918 ± 0.033	AC-AW
5650.648	−27.370	8.713	0.940 ± 0.024	AC-AE
5650.648	−50.557	8.809	0.972 ± 0.063	AC-E6
5650.648	77.011	5.821	0.815 ± 0.044	AW-E6
5650.648	26.453	14.630	0.939 ± 0.034	AC-AW
5650.658	−27.217	8.478	0.967 ± 0.022	AC-AE
5650.658	−49.982	8.375	0.909 ± 0.044	AC-E6
5650.658	75.361	6.478	0.793 ± 0.026	AW-E6
5650.658	25.379	14.853	0.906 ± 0.030	AC-AW
5653.629	−27.424	8.992	0.909 ± 0.030	AC-AE
5653.629	−51.003	9.326	0.824 ± 0.047	AC-E6
5653.629	78.603	5.029	0.734 ± 0.070	AW-E6
5653.629	27.599	14.355	0.879 ± 0.040	AC-AW
5653.636	−27.406	8.814	0.922 ± 0.029	AC-AE
5653.636	−50.748	8.995	0.805 ± 0.080	AC-E6
5653.636	77.631	5.537	0.780 ± 0.067	AW-E6
5653.636	26.883	14.532	0.914 ± 0.050	AC-AW
5653.645	−27.302	8.589	0.940 ± 0.026	AC-AE
5653.645	−50.277	8.580	0.835 ± 0.063	AC-E6
5653.645	76.175	6.169	0.755 ± 0.065	AW-E6
5653.645	25.899	14.748	0.933 ± 0.041	AC-AW
5653.647	−27.261	8.532	1.027 ± 0.064	AC-AE
5653.647	−50.130	8.475	0.846 ± 0.056	AC-E6
5653.647	75.764	6.328	0.807 ± 0.055	AW-E6
5653.647	25.634	14.802	0.933 ± 0.037	AC-AW
5653.656	−27.064	8.325	0.919 ± 0.038	AC-AE
5653.656	−49.507	8.094	0.816 ± 0.055	AC-E6
5653.656	74.132	6.900	0.742 ± 0.080	AW-E6
5653.656	24.625	14.994	0.937 ± 0.035	AC-AW
5656.633	−27.358	8.688	0.950 ± 0.026	AC-AE
5656.633	−50.504	8.761	0.842 ± 0.037	AC-E6
5656.633	76.844	5.893	0.788 ± 0.022	AW-E6
5656.633	26.341	14.654	0.936 ± 0.022	AC-AW
5656.641	−27.232	8.495	0.911 ± 0.030	AC-AE
5656.641	−50.030	8.407	0.883 ± 0.040	AC-E6
5656.641	75.490	6.430	0.777 ± 0.043	AW-E6

Table 5. Continued.

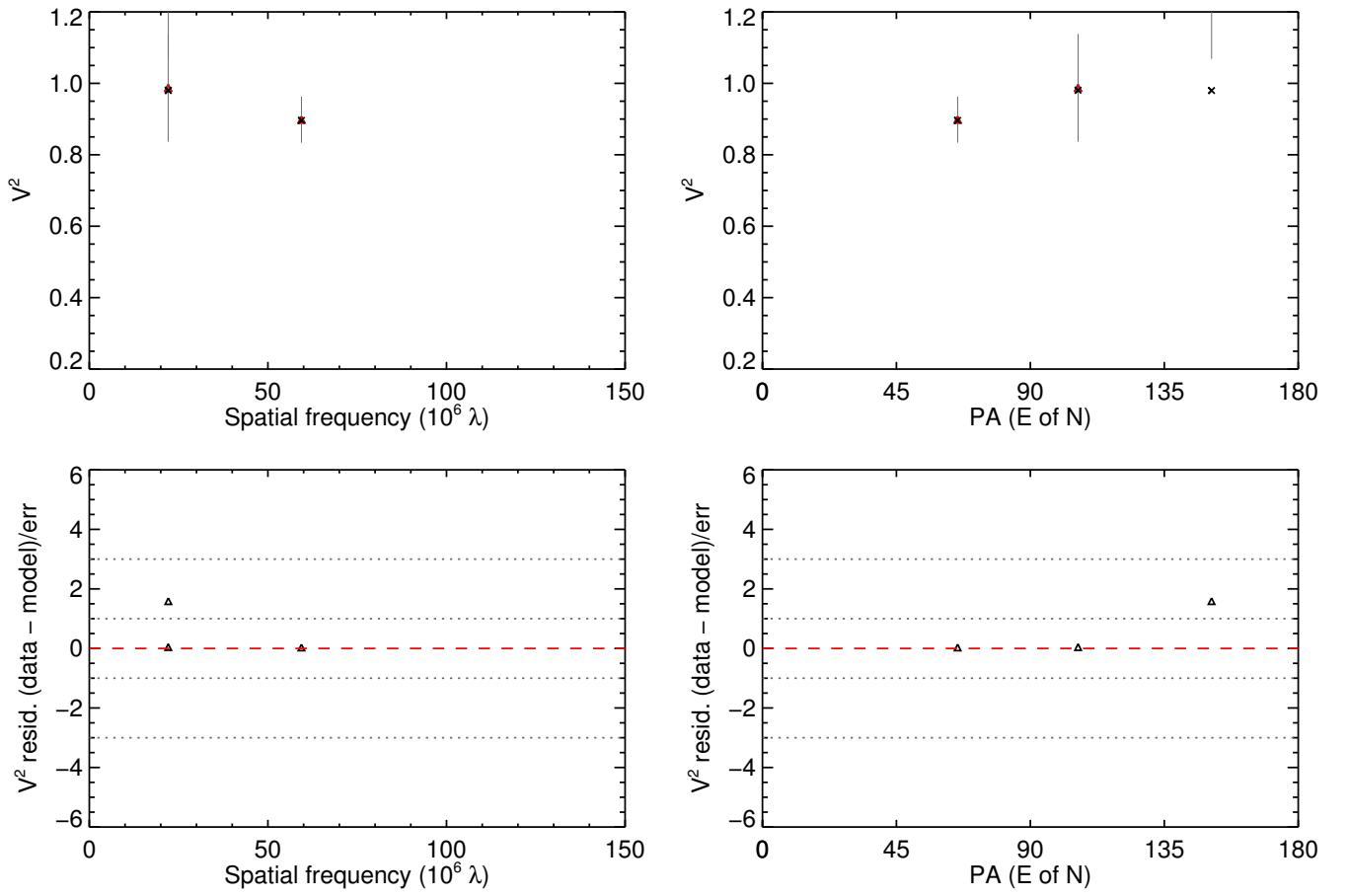| Julian Date (JD - 2 450 000)	Spatial Frequency u (10^6 cycles rad^{-1})	Spatial Frequency v (10^6 cycles rad^{-1})	V^2	Baseline
5656.641	25.460	14.837	0.919 ± 0.028	AC-AW

Fig. 12. The FSU-A *K*-band squared visibilities (red with gray error bars) and the corresponding parametric ($n = 3.5$) model predictions (black).
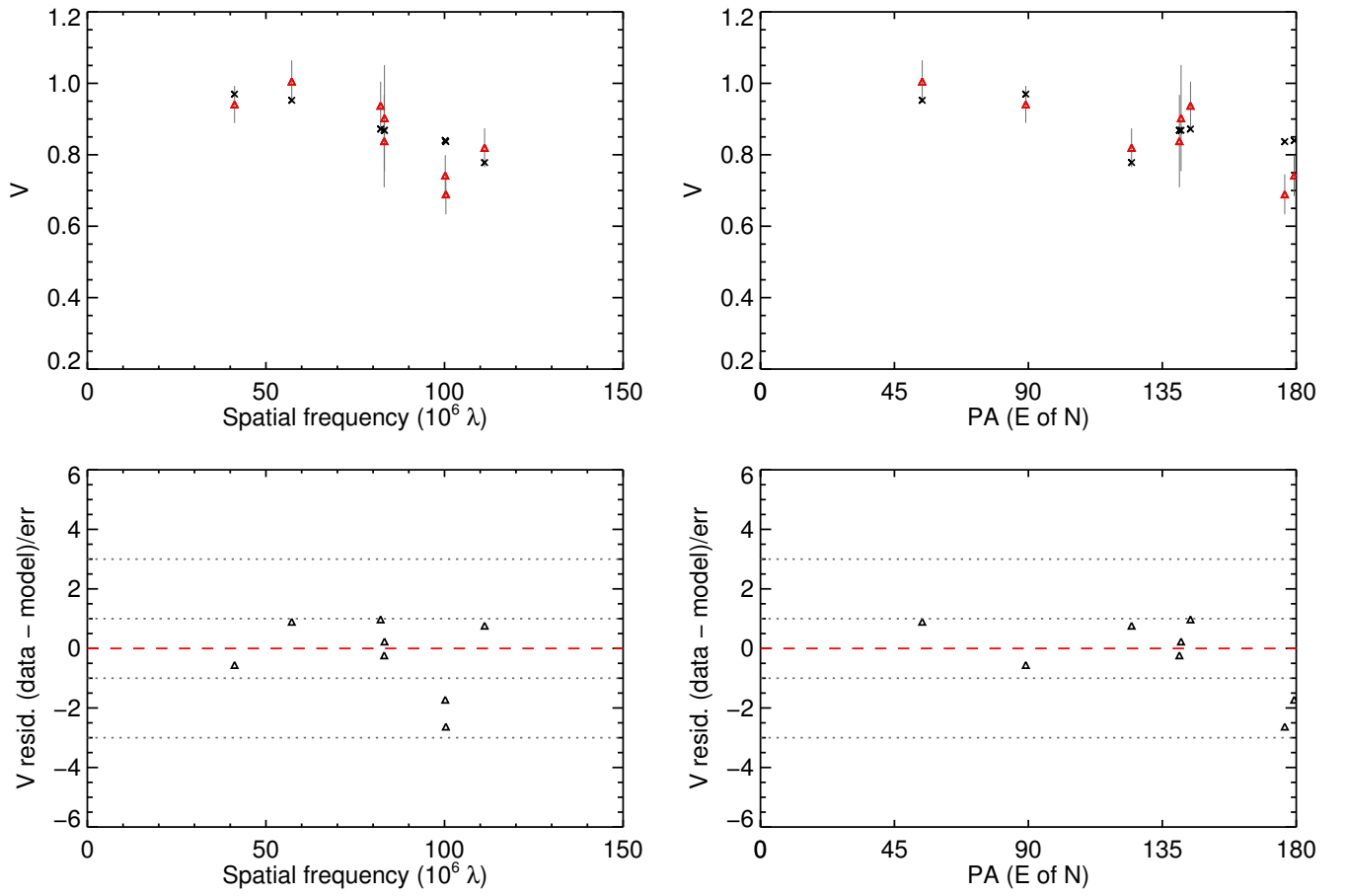
Fig. 14. The CLIMB *K*'-band visibilities (red with gray error bars) and the corresponding parametric (*n* = 3.5) model predictions (black).